UNIVERSITÀ
DEGLI STUDI
FIRENZE

UNIVERSITÀ DEGLI STUDI DI FIRENZE
DIPARTIMENTO DI INGEGNERIA DELL'INFORMAZIONE (DINFO)
CORSO DI DOTTORATO IN INGEGNERIA DELL'INFORMAZIONE

CURRICULUM: ELETTRONICA ED ELETTROMAGNETISMO
SSD: ING-INF/01

NOVEL ULTRASOUND IMAGING TECHNIQUES

Candidate
Valentino Meacci

Supervisors
Prof. Piero Tortoli

Prof. Stefano Ricci

PhD Coordinator
Prof. Luigi Chisci

PhD CYCLE XXIX, 2013-2016

Università degli Studi di Firenze, Dipartimento di Ingegneria
dell'Informazione (DINFO).

November 2016

Acknowledgments

I would like to sincerely thank my supervisors, Prof. Piero Tortoli and Ing. Stefano Ricci for their time, and their knowledgeable advices. A Special thank goes to my wonderful family for their love and support over the years. Lastly, a thank to my lab mates for the jokes, the distractions, the good times, and their great help and support.

Contents

Chapter 1. **Introduction**

1.1. Objective

Ultrasound Imaging is widely used in biomedical and industrial applications, due to its non-invasive, non-destructive and non-ionizing nature. In the last 20 years, Ultrasound imaging has been continuously growing in both of these fields, since it has benefited from advances in electronic technologies and in signal processing methods.

For industrial applications, a wide variety of instruments, based on ultrasound, have been designed to measure the properties and composition of materials and products. In particular, monitoring all of the steps of a production chain is crucial for process optimization and product quality in industries. In the medical area, ultrasound systems are widely used to investigate the tissue, by 2D morphological imaging, and the blood movement, by Doppler analysis. The large use of ultrasound equipment has further increased the research and the development activity of new investigation methods. Consequently, "open" systems capable of satisfying the research needs are in great demand.

The activity of this PhD was focused on the design of new electronic architectures and systems capable of addressing some of the emerging needs in medical and industrial fields.

Industrial applications

In several industrial fields the products are checked by taking samples from the production chain, which are lately analyzed in specialized laboratories by using manual, expensive and time consuming operations. Systems capable of in-line and on-site monitoring products and materials would be of high value. For these reasons, we developed an ultrasound system for monitoring the properties of the fluids or suspensions flowing in pipes and another system to assess the concrete strength during the hydration process.

The first one is a system with a wide range of applications, since a lot of products as food, medicines and cosmetics are in a fluid or suspension state during the production. It is a pulse wave system that measures the velocity profile of the fluids flowing in a pipe and uses the relation between the velocity profile and the fluid rheological properties to evaluate the quality of the products and keep the production chain under control.

The second system evaluates the concrete strength, a parameter of paramount importance to guarantee durable and safe constructions. It is a pulse wave system that exploits a reflectometry technique to monitor the concrete strength evolution during the hardening process by analyzing the reflected signal at interface concrete-Plexiglas.

Medical applications

In medical applications, High Frame Rate (HFR) imaging methods based on the transmission of defocused, plane-wave (PW) or multi-focused beams rather than single-focused beams, are increasingly popular. These methods lead to unprecedented performance that enables the reconstruction of 2D vector maps of the blood velocity distribution, or 3D investigations with improved resolution, but they are unfortunately very demanding in term of processing power. Therefore, the design and development of novel HFR methods and systems capable to efficiently implement the HFR imaging methods, is a crucial challenge. Toward this goal the Micro Systems Design Laboratory (MSD Lab) of the University of Florence developed a novel research scanner called ULtrasound Advanced Open Platform 256 (ULA-OP 256). ULA-OP 256 can independently manage up to 256 transmit/receive (TX-RX) channels. It has high computational power in a small size, compatible with mobility. The system supports a wide range of transmission/receiving strategies, processes data in real time, stores data for post-processing, and can be connected to matrix probes. In particular, the platform implements an advanced beamformer architecture, named Multi-Line Parallel Beamformer (MLPBF). MLPBF exploits a combination of parallel and serial processing strategies that make HFR imaging possible.

The manuscript is organized as follows:

•Chapter 2: The fundamental concepts of ultrasonic wave propagation, the characteristic parameters of propagation media and the effects that they generate are briefly described. The main features of single element and array transducers are reported. Basics on ultrasound systems and signal elaboration are summarized.

•Chapter 3: A brief introduction about concrete properties and methods used to measure the concrete strength are presented. The architecture of the ultrasound system designed in our lab is detailed. The measurements setup and results are reported.

•Chapter 4: An introduction about fluids/suspensions properties and classical techniques used for assessing rheological properties of the opaque fluids are presented. The ultrasound system designed in our lab is described in detail. Experimental setups and tests performed in the MSD Lab and in industrial environments are reported.

•Chapter 5: A novel hardware architecture called MLPBF for High Frame Rate imaging is presented. It is shown that the image frame rate can be improved by using a combination of serial and parallel elaboration. The architecture was implemented on the research ultrasound scanner ULA-OP 256, whose features are presented in detail. The results obtained by MLPBF are finally compared with those obtained by a standard method.

1.2. Contributions

Conference Proceedings

- **Meacci, V.**, Bassi, L., Ricci, S., Boni, E., Tortoli, P.: Compact hardware for real-time multi-line beamforming. 2014 IEEE International Ultrasonics Symposium (IUS) Proceedings, pp. 1245-1248 (2014).

- Wiklund, J., Kotzé, R., Birkhofer, B., Ricci, S., **Meacci, V.**, Haldenwang, R., Stading, M.: Flow-VizTM–A fully integrated and commercial in-line fluid characterization system for industrial applications. 2014 9th International Symposium on Ultrasonic Doppler Methods for Fluid Mechanics and Fluid Engineering (ISUD) Proceedings. pp. 165-168 (2014).

- Boni, E., Bassi, L., Dallai, A., Giannini, G., Guidi, F., **Meacci, V.**, Matera, R., Ramalli, A., Ricci, S., Scaringella, M., Viti, J., Tortoli, P.: ULA-OP 256: A portable high-performance research scanner. 2015 IEEE International Ultrasonics Symposium (IUS) Proceedings, pp. 1245-1248 (2015).

- Ricci, S., **Meacci, V.**, Birkhofer, B., Wiklund, J.: Embedded system for in-line ultrasound velocity profile detection. 2015 IEEE International Ultrasonics Symposium (IUS) Proceedings, pp. 1–4 (2015).

- Boni, E., Bassi, L., Dallai, A., Giannini, G., Guidi, F., **Meacci, V.**, Ramalli, A., Ricci, S., Tortoli, P.: Open Platforms for the Advancement of Ultrasound Research. 2016 Applications in Electronics Pervading Industry, Environment and Society. pp. 59–64. Springer International Publishing (2016).

- **Meacci, V.**, Ricci, S., Wiklund, J., Birkhofer, B., Kotze, R.: Flow-Viz - An integrated digital in-line fluid characterization system for industrial applications. 2016 IEEE Sensors Applications Symposium (SAS) Proceedings, pp. 1–6 (2016).

- **Meacci, V.**, Bassi, L., Ricci, S., Boni, E., Tortoli, P.: High-Performance FPGA Architecture for Multi-Line Beamforming in Ultrasound Applications. 2016 Euromicro Conference on Digital System Design (DSD). pp. 584–590 (2016).

- **Meacci, V.**, Ricci, S., Bruehwiler, A., Lootens, D.: Compact ultrasound board for measurement of concrete compressive strength. 2016 IEEE International Ultrasonics Symposium (IUS) Proceedings, pp. 1–4 (2016).

- Boni, E., Bassi, L., Dallai, A., **Meacci, V.**, Ramalli, A., Scaringella, M., Guidi, F., Ricci, S., Tortoli, P.: A real-time beamformer for high frame rate ultrasound imaging. 2016 IEEE International Ultrasonics Symposium (IUS) Proceedings, pp. 1–4 (2016).

- Ramalli, A., Dallai, A., Boni, E., Bassi, L., **Meacci, V.**, Giovannetti, M., Tong, L., D'hooge, J., Tortoli, P.: Multi transmit beams for fast cardiac imaging towards clinical routine. 2016 IEEE International Ultrasonics Symposium (IUS) Proceedings, pp. 1–4 (2016).

- Ricci, S., Bassi, L., **Meacci, V.**, Ramalli, A., Boni, E., Tortoli, P.: Multiline Measurements of Blood Velocity Vectors in Real-Time. 2016 IEEE International Ultrasonics Symposium (IUS) Proceedings, pp. 1–4 (2016).

- Wiklund, J., Ricci, S., **Meacci, V.**, Kotze, R., Birkhofer, B.: Flow-Viz Pulsed Ultrasonic Doppler System with Auto Tuning of Analog-, Digital Gain and Threshold. 2016 10th International Symposium on Ultrasonic Doppler Methods for Fluid Mechanics and Fluid Engineering (ISUD) Proceedings, pp. 241-248 (2016).

- **Meacci, V.**, Ricci, S., Bruehwiler, A., Lootens, D.: Non Destructive Ultrasound Equipment to Evaluate the Concrete Compressive Strength. Applications in Electronics Pervading Industry, Environment and Society. (In press).

- Ricci, S., **Meacci, V.**, Birkhofer, B., Wiklund, J.: Embedded System for In-Line Characterization of Industrial Fluids. Applications in Electronics Pervading Industry, Environment and Society. (In press).

Journal papers

- Wiklund, J., Birkhofer, B., Ricci, S., **Meacci, V.**, Stading, M.: An integrated in-line fluid characterization system for industrial applications. Journal of Japan Society of Fluid Mechanics 34, 241–248(2015).

- Boni, E., Bassi, L., Dallai, A., Guidi, F., **Meacci, V.**, Ramalli, A., Ricci, S., Tortoli, P.: ULA-OP 256: A 256-Channel Open Scanner for Development and Real-Time Implementation of New Ultrasound Methods. IEEE Transactions Ultrasonics and Ferroelectric, and Frequency Control. 63, 1488–1495 (2016).

- Ricci, S., **Meacci, V.**, Birkhofer, B., Wiklund, J.: FPGA-based System for In-Line Measurement of Velocity Profiles of Fluids in Industrial Pipe Flow. IEEE Transactions on Industrial Electronics. 99, 1-1 (2016).

Chapter 2. Ultrasounds Basics

This chapter gives a brief survey of Ultrasound Waves, Ultrasound Pulse Wave Systems and Ultrasound Transducers. The first part of the chapter introduces a math model suitable to describe the ultrasound waves propagation, the second part deals with the transducers and how they work, finally, the third part describes the Ultrasound Pulse Wave systems.

2.1. Ultrasound waves

Ultrasounds consists in mechanical waves that propagate in a medium constituted by fluids, solids or gases at the frequency above the range of the human hearing (Upper limit 20 kHz) [1]. These waves generate a perturbation of the medium particles, which interact with their neighbors to transmit the perturbation. Ultrasound waves propagate in three modes that are based on the way the particles move:

- Longitudinal waves;
- Shear waves;
- Surface waves.

In longitudinal waves, the medium particles move in the direction of wave propagation. Since compressional and dilatational forces are active in these waves, they are also called pressure or compressional waves. In the shear wave, the particles move along right angle or transverse to the propagation direction. Surface waves travel on the surface of a material penetrating to a depth of one wavelength. The waves propagation depends on the elastic properties of the medium as well as its mass density.

Linear propagation corresponds to waves propagation inside the medium without changes in the shape of the waves. Nonlinear propagation is present when the shape and amplitude change during the waves propagation losing proportionality to the input excitation.

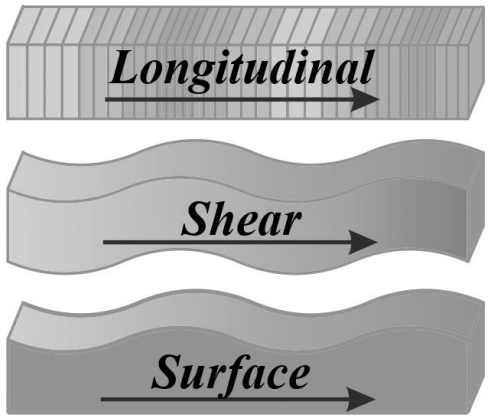

Fig. 1: Longitudinal, Shear and Surface Ultrasound Waves.

2.1.1. Linear Propagation

Linear propagation of ultrasound waves can be described using the wave equation when three fundamentals principles are respected:

- Conservation of the mass;
- Conservation of momentum;
- Equation of state or pressure-density relation. The pressure-density relation must be linear.

The partial differential equation of a wave propagating along the z direction is:

$$\frac{1}{c^2}\frac{\partial^2 p_a}{\partial t^2} = \frac{\partial^2 p_a}{\partial z^2} \quad (1)$$

Where p_a is the acoustic pressure and *c* the sound speed in the medium. The solution of (1) is:

$$p_a(z,t) = p_0 e^{j(kz \pm 2\pi f t)} \quad (2)$$

Where f is the frequency, $k = 2\pi/\lambda$ is the wave number, λ is the wave length, and p_0 the amplitude of the wave at z=0.

The propagation speed of acoustic waves *c*, is strictly dependent on the elastic properties and the density of the medium and can be expressed as:

$$c = \sqrt{\beta/\rho} \quad (3)$$

Where ρ is the volumetric medium density and β is a bulk modulus that describes how the density changes in relation with the pressure.

Another important material property is the acoustic impedance *Z*, which for a propagating mechanical wave, is expressed as:

$$Z = \rho c \quad (4)$$

2.1.2. Non-Linear Propagation

For large amplitude waves, the three fundamentals principles reported above are not necessary true, and the wave propagation is described as nonlinear.

The speed of the mechanical wave in a nonlinear medium isn't constant but changes in relation with the pressure. If $|v_a|$ is the velocity of the particle and it is a significant percentage of *c*, the part of the wave at higher pressure move with speed $c + |v_a|$ and those at lower pressure at $c-|v_a|$. Moreover, when the medium

is compressed, the bulk modulus increase and vice versa; therefore, the sound speed will be faster at higher pressure and slower at lower pressure.

The harmonic generation is the most important effect produced by nonlinearity. The wave shape changes: if the original signal is a sine wave with a frequency f_0, during nonlinear propagation the energy will be shifted into multiples of this fundamental frequency, nf_0 called harmonics, where *n* is a positive integer.

The nonlinear pressure-density is obtained by expanding the linear pressure-density relation $p_a = c_0^2 \rho_a$ with a term of the Taylor series around a point (p_0, ρ_0) :

$$\begin{cases} p_a = A\left(\frac{p_a}{\rho_0}\right) + \frac{B}{2!}\left(\frac{p_a}{\rho_0}\right)^2 + .. \\ A = \rho_0 \left(\frac{\partial p}{\partial \rho}\right) = \rho_0 {c_0}^2 \\ B = {\rho_0}^2 \left(\frac{\partial^2 p}{\partial \rho^2}\right) \end{cases} \quad (5)$$

Where c_0 is the sound speed at the density ρ_0.The ratio *B/A* is the nonlinearity parameter and it quantifies the nonlinearity in acoustical propagation.

The wave propagation velocity in nonlinear medium can be written:

$$c = c_0 + \left(\frac{B}{2A}\right) v_a \quad (6)$$

Finally, the coefficient of nonlinearity is defined as:

$$\beta = 1 + \frac{B}{2A} \quad (7)$$

2.1.3. Waves Reflection

When a wave encounters a boundary or impedance discontinuity, part of it is reflected and part transmitted, see Fig. 2. The incident wave, reflected wave and transmitted wave must conform to two conditions:

- The acoustic pressure on the both side of the boundaries must be equal;
- The particle velocities normal to the boundaries must be equal.

The incidence angle θ_i and the transmittance angle θ_t are related through the Snell's law:

$$\frac{sin(\theta_i)}{c_1} = \frac{sin(\theta_t)}{c_2} \quad (8)$$

$$\theta_i = \theta_r \tag{9}$$

where θ_r is the reflected angle.:

$$\begin{cases} p_t = p_i + p_r \\ v_t\, cos(\theta_t) = v_i\, cos(\theta_i) + v_r \cos(\theta_r) \end{cases} \Rightarrow$$
$$\Rightarrow \frac{\mathrm{p_t}}{\mathrm{v_t}} = \frac{(p_i + p_r) cos(\theta_t)}{v_i\, cos(\theta_i) + v_r cos(\theta_r)} \tag{10}$$

Where p_i, p_t and p_r are the incident, transmitted and reflected pressures, and v_i, v_t and v_r are the incident, transmitted and reflected velocities. Finally, the transmission and reflection coefficients are:

$$R(\theta_i) = \frac{p_r}{p_i} = \frac{\rho_2 c_2 \cos(\theta_i) - \rho_1 c_1 \cos(\theta_t)}{\rho_2 c_2 \cos(\theta_i) + \rho_1 c_1 \cos(\theta_t)} \tag{11}$$

$$T(\theta_i) = \frac{p_t}{p_i} = \frac{2\rho_2 c_2 \cos(\theta_i)}{\rho_2 c_2 \cos(\theta_i) + \rho_1 c_1 \cos(\theta_t)} \tag{12}$$

When acoustic pressure is normally incident on the boundary, the coefficients *T* and *R* become:

$$T = \frac{2\rho_2 c_2}{\rho_2 c_2 + \rho_1 c_1} = \frac{2Z_2}{Z_2 + Z_1} \tag{13}$$

$$R = \frac{\rho_2 c_2 - \rho_1 c_1}{\rho_2 c_2 + \rho_1 c_1} = \frac{Z_2 - Z_1}{Z_2 + Z_1} \tag{14}$$

When the incidence angle is such that $\sin(\theta_i) = c_1/c_2$ the critical angle is reached and the transmitted wave travels along the interface. If the incidence angle becomes larger than the critical angle, the wave is totally reflected and the reflection coefficient becomes $|R|=1$.

2.1.4. Wave Refraction

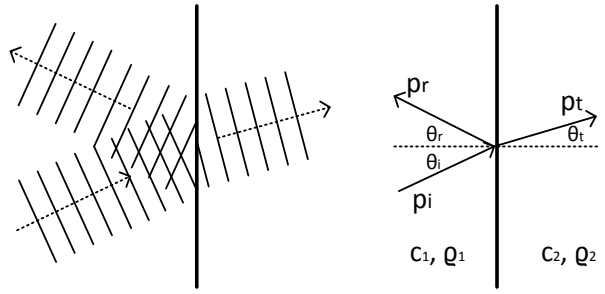

Fig. 2: Plane wave Reflection and transmission with incident angle θ_i

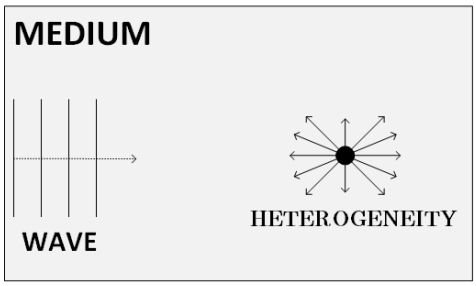

Fig. 3: Heterogeneity in the medium and scattering phenomena

Refraction is a phenomenon that occurs when a wave travels from one medium to another with a different sound speed. In this case the wave direction and wavelength change. Huygens' Principle can be used to show in which direction the wave travels in the new medium. When a wave travels into a medium with a slower sound speed the direction of the wave will move closer to the normal, otherwise when a wave moves into a faster medium, it will bent away from the normal.

- If $c_2 < c_1$ the direction of propagations moves toward the normal to the boundary;
- If $c_2 > c_1$ the direction of propagations moves away the normal to the boundary.

2.1.5. Scattering and Diffraction

The Scattering is depicted in Fig. 3 and it's the most important nonlinear phenomenon and has a main importance in ultrasound imaging. Scattering is composed by reflection and diffraction caused by heterogeneities of the medium that deflect the wave energy in multiple directions. The diffraction occurs when a wave encounters an obstacle, and 'bend' around its corner. In Fig. 4 three examples of diffraction are reported, at a corner, through an aperture and past an obstacle.

2.1.6. Absorption and Attenuation

When the ultrasound wave travels inside the medium, its energy is partially lost due two phenomena:

- Absorption: refers to the dissipation (conversion) of acoustic energy into heat;
- Attenuation: refers to any reduction in the amplitude of wave due to reflection, scattering, etc.

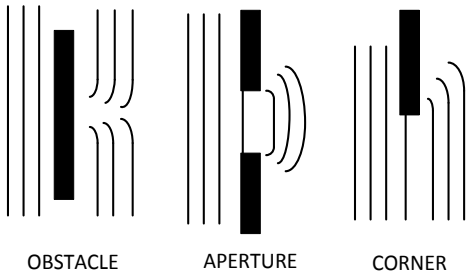

Fig. 4: Wave diffraction on an obstacle, an aperture and a corner.

A plane wave that propagates in the medium with non-zero absorption suffers of a reduction of amplitude and an additional exponential-decay factor must be add to the wave equation. A wave that propagates along z-axis is described by the following equation with the additional factor:

$$p_a(z,t) = p_0 e^{j(kz \pm 2\pi f t)} e^{-j\alpha z} \quad (15)$$

Where α is the medium absorption coefficeint.

2.2. Transducers

The probes used in this work are composed of Piezoelectric Transducers (PZT), that uses the piezoelectric effect to convert the electric signal to mechanical energy and transmit mechanical waves. The opposite process can be used to convert mechanical energy to electric signal.

2.2.1. PZT Transducers

A piezoelectric material is characterized by an arrangement of the electrical dipoles along one direction (usually the z axis direction). When a traction or compression is applied on the face of the piezoelectric crystal, on one surface appear a net positive charge and a net negative charge on the other surface, therefore a potential difference is created across the element. Otherwise, when a voltage is applied across the crystal, a mechanical contraction or expansion of the transducer elements is obtained. The operating frequency f_0 is determined from the speed of sound in the medium c, and the thickness t of the piezoelectric material: $f_0 = c/2t$. The "*Q factor*" describes the bandwidth of the acoustic wave emitted by a transducer as:

$$Q = \frac{f_0}{Bw} \quad (16)$$

Where Bw is the bandwidth computed at -3 dB.

The simplest probe is a piezoelectric element with electrodes on the sides. The behavior of the piezoelectric element is described by the material constitutive equations:

$$\begin{cases} S = s^E T + d^T E \\ D = dT + \varepsilon^T E \end{cases} \quad (17)$$

Where S is the mechanical strain, T is the mechanical stress, D is the electrical displacement (charge density), E is the electric field, s^E is the compliance under a zero or constant electrical field and ε^T is the dielectric permittivity under a zero or constant stress, d and d^T are the matrices accounting the piezoelectric effect.

In Fig. 5, a piezoelectric transducer array is showed; every array element has a backing material on the rear face and a matching layer on the emitting face. The acoustic impedance of the matching layer is between the impedance of the active elements and the impedance of the medium in which the acoustic wave is emitted to optimize energy transfer. Usually, the thickness of the matching layer is 1/4 of the wavelength to keep the reflected waves within the matching layers in phase with the transmitted wave (wave guide λ/4).

The backing acoustic impedance is designed to smooth the ripple in the transducer bandwidth and absorb the wave for avoiding influence on the transmitted signals. This damping characteristic improves the axial resolution, because the wave transmitted in the back direction can't be reflected.

The elements are defined by length (*L*), width (*W*), pitch or periodicity (*p*) and the space between elements or *"kerf"*, see Fig. 6. The elements are covered by a cylindrical lens for elevation focusing and are electrically connected to the system through a cable.

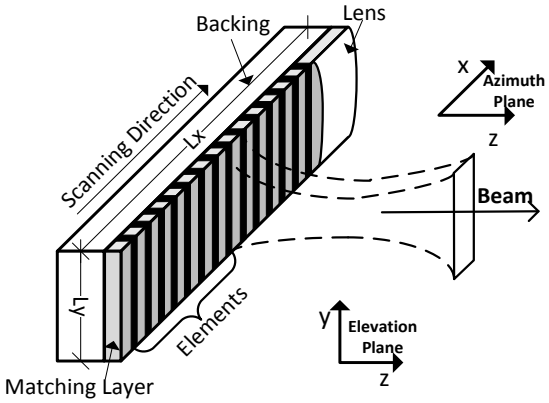

Fig. 5: Construction of 2D array probe

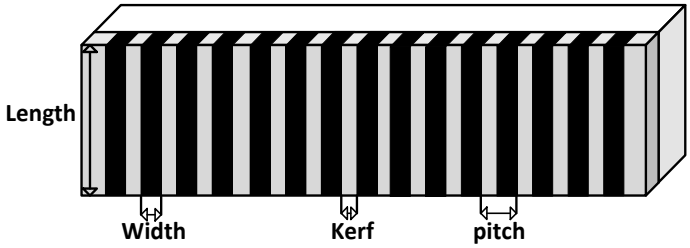

Fig. 6: Active elements dimensions.

Normally the azimuth plane XZ can be scanned electronically and the lens set the fixed focal length in the YZ plane. Typically, the shape of elements is rectangular as depicted in the Fig. 6.

2.2.2. Array Theory

To understand the beam pattern generated by an array composed of elements with aperture L_x, L_y of the order of a wavelength, see Fig. 7, the aperture function of the single element, that describes far field radiation, must be considered [1]:

$$A(x_0, y_0, 0) = sinc\left(\frac{x_0}{L_x}\right) sinc\left(\frac{y_0}{L_y}\right) \quad (18)$$

The far-field beam pattern for an aperture of size L_x and L_y, in the far field, can be found from the Fourier transforms of the aperture function:

$$H_e(x, y, z, \lambda) = \frac{c_0}{2\pi z} L_x sinc\left(\frac{L_x x}{x\lambda_z}\right) L_y sinc\left(\frac{L_y y}{y\lambda_z}\right) \quad (19)$$

Considering the spherical coordinate geometry, each point of the field is described by

$$u = sin\theta cos\phi \quad (20)$$

$$v = sin\theta sin\phi \quad (21)$$

Where θ is the angle between z and r, and ϕ is the angle between x and r, as depicted in Fig. 7. The far-field beam pattern in spherical geometry is:

$$H_e(x, y, z, \lambda) = \frac{c_0}{2\pi r} L_x sinc\left(\frac{L_x u}{\lambda}\right) L_y sinc\left(\frac{L_y v}{\lambda}\right) \quad (22)$$

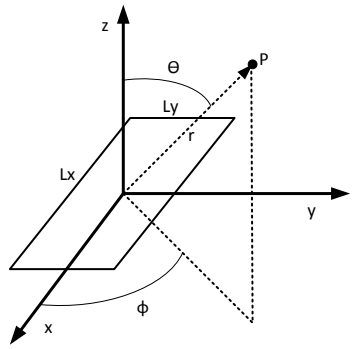

Fig. 7: Single active element with aperture on the order of wavelength.

The time domain equivalent of (22) can be found from the inverse Fourier transform with $\lambda = c/f$.

$$h_e(u,v,r,t) = \\ = \frac{c_0}{2\pi r} L_x\left(\frac{c}{L_x u}\right)\prod\left(\frac{t}{L_x u/c}\right) * L_x\left(\frac{c}{L_y v}\right)\prod\left(\frac{t}{L_y v/c}\right) \qquad (23)$$

This convolution of two rectangles has the trapezoidal shape illustrated in the Fig. 8 and represents the spatial impulse response of a rectangular array element in spherical coordinate.

For a typically two-dimensional beam scanning (XZ plane), the array elements will extend along the x axis, therefore H_x in (22) can be expressed as a function of frequency:

$$H_x(\theta,r,f) = h_{0x} L_x sinc\left(\frac{L_x f\ sin\theta}{c}\right) \qquad (24)$$

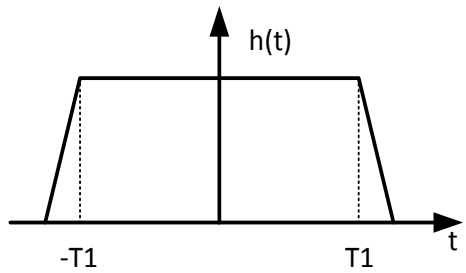

Fig. 8: Far field impulse response for rectangular array element.

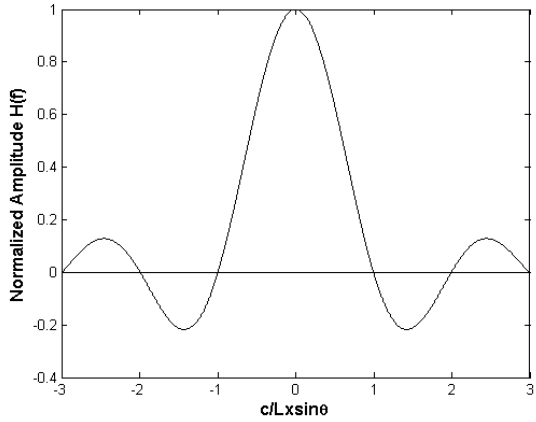

Fig. 9: Element directivity as function of frequency for an element with length L_x .

where $h_{0x} = \sqrt{c_0/2\pi r}$. This function is plotted in Fig. 9 and represents the element directivity as a function of frequency for an element length L_x. Its far-field time response is the inverse Fourier transform:

$$h_x(\theta, r, t) = h_{0x} L_x \left(\frac{c}{L_x \sin\theta}\right) \prod \left(\frac{t}{L_x \sin\theta / c}\right) \qquad (25)$$

The pressure pulse, in the far field of an element in the scan (XZ) plane for a pulse excitation, with frequency 2 MHz and parameter *a*=1 is depicted in Fig. 10 and expressed by a decaying exponential function *g(t):*

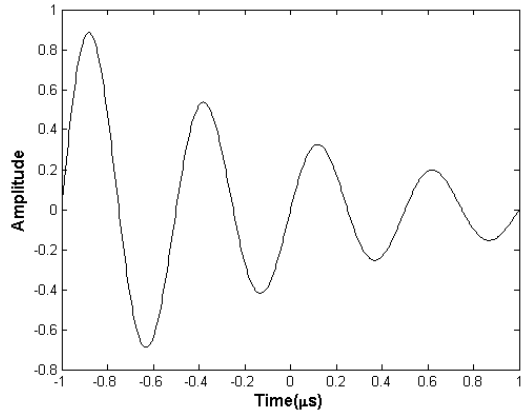

Fig. 10: Typical acoustical excitation signal.

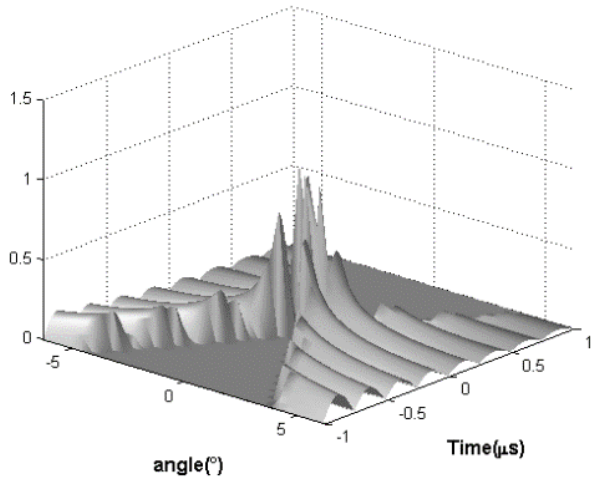

Fig. 11: Absolute value of pressure, waveform as a function of angle and time.

$$g(t) = g_0 e^{-at} \cos(\omega t)\, H(t) \qquad (26)$$

Where g_0 is the amplitude at $t = 0$ and *H(t)* is the Heaviside function. The convolution of the pulse excitation and the far-field time response of the piezoelectric element can be used to obtain the pressure impulse in the far field, reported in Fig. 10 :

$$p(r,t) = p_0 g(t) * h_{0x} L_x \left(\frac{c}{L_x\, sin\theta}\right) \prod \left(\frac{t}{L_x\, sin\theta / c}\right) \qquad (27)$$

Fig. 11 reports the absolute values of pressure waveforms as a function of angular direction and time. They are plotted in an isometric presentation over a small angular range: -6.25° to 6.25° with an increment of 0.4°, for the pulse of 4-cm-long aperture.

An ideal, infinite array composed by spatial points is a good starting point to represent an array of elements. Each point can be represented by a Dirac comb with a periodicity *p*, as depicted in Fig. 12(a). The Fourier transform is related to the pressure at a field point. The result is another Dirac comb with a periodicity (λ/p), see Fig. 12(b):

$$\Im\left[p\mathrm{III}\left(\frac{x}{p}\right)\right] = p\mathrm{III}\left(\frac{puf}{c_0}\right) = p\mathrm{III}\left(\frac{u}{\lambda/p}\right) \qquad (28)$$

For an aperture of finite length L_x, see Fig. 13, the infinite sum of the Dirac comb is reduced to finite in the spatial *Lx* domain, and the Fourier transform as is given as follows:

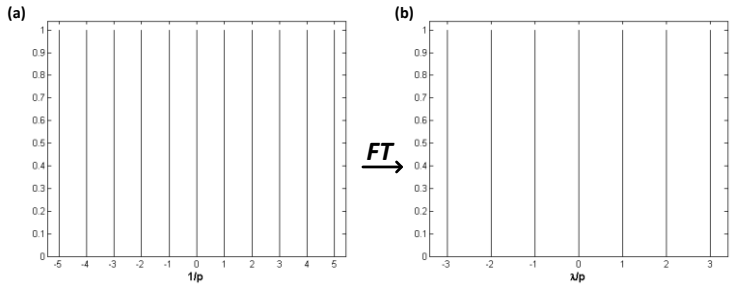

Fig. 12: Ideal Elements Dirac comb (a), Fourier transform related to the pressure at a field point (b)

$$\Im\left[\prod\left(\frac{x}{L_x}\right) p\mathrm{III}\left(\frac{x}{p}\right)\right] = pL_x \sum_{-\infty}^{\infty} sinc\left[\frac{L_x}{\lambda(u-m\lambda/p)}\right] = L_x sinc\left[\frac{L_x u}{\lambda}\right] * p\mathrm{III}\left(\frac{u}{\lambda/p}\right) \quad (29)$$

In the frequency domain, the main lobe is at $m = \pm 1$ centered in $u = 0$, the others, called grating lobes, are at $m \neq 0$ and centered on direction at angles:

$$\theta_g = \pm arcsin(m\lambda/p) \quad (30)$$

The number of grating lobes depend on the periodicity p *(e.g.* for $p = 2\lambda$ there are two grating lobes located at $\pm 30°$) .

To consider the real shape of the elements, the point sources can be replaced by rectangular elements with width *w*. In a spatial domain, the Dirac comb are subsisted by rectangular functions with pitch p/λ and width w/λ, as showed in Fig. 14(a). The Fourier transform is:

$$H_0(u,\lambda) = h_0 \Im\left[\prod\left(\frac{x}{w}\right) * \sum_{-nL}^{nL} \delta(x - np)\right] = \sum_m h_{0x} L_x pw\, sinc\left(\frac{wu}{p}\right) sinc\left[\frac{L_x}{\lambda(u - m\lambda/p)}\right] \quad (31)$$

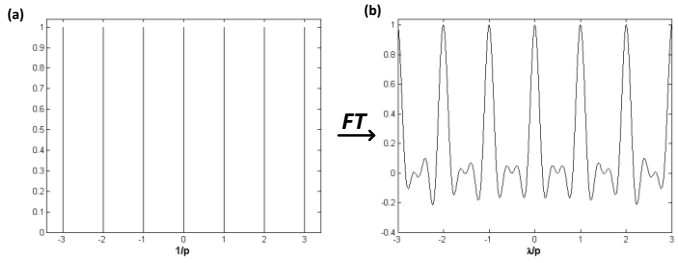

Fig. 13: Ideal Elements Dirac comb (a), Fourier transform related to the pressure at a field point (b), both for array with aperture Lx

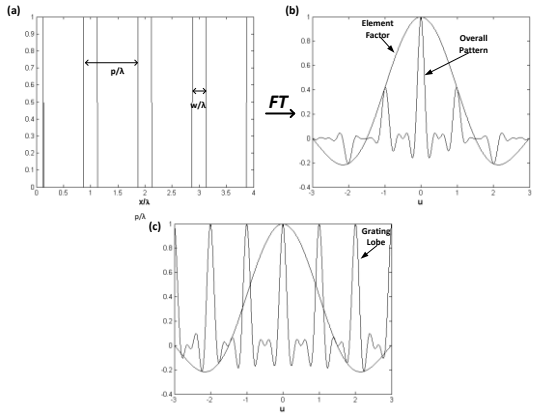

Fig. 14: Rectangular elements of width w(a). Fourier transform modulated by element factor(b); Factors contributing to overall transform(c).

The first *sinc* term is the element factor, it depends on the element size and influences the directivity by modulating the sequence of grating lobes, as shown in Fig. 14(b).

Another feature of the array is the Beam steering used to change a direction of the waves front and direct the beam to a specific location in the zone of interest. In Fig. 15 the beam steering due to the effect of the linear phase τ_{sn} that steers a beam at an angle θ from the z axis is reported.

This phase is applied, one element at a time, as a linear phase factor $u_s = sin\theta$:

$$e^{-(i\omega_c\tau_{sn})} = e^{-(i2\pi f_c(npu_s)/c)} = e^{(-i2\pi(npu_s)/\lambda_c)} \qquad (32)$$

In sector or angular scanning, the location of the grating lobe is related to the steering angle:

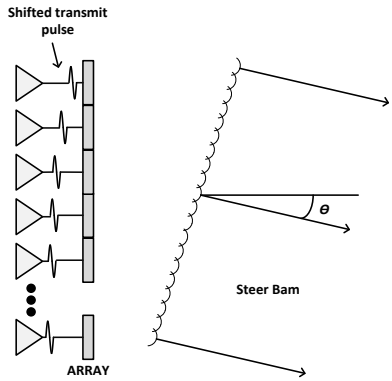

Fig. 15: Delayed excitation signals to steer wave front.

$$\theta_g = \pm \arcsin(m\lambda/p - u_s) \quad (33)$$

The first grating lobes are at $m = \pm 1$.

2.3. Ultrasound Beamforming

The beamforming is a technique widely used in ultrasound systems to focalize and steer the beams by the control of the delay and weighting of the signal from each element of the probe [2].

During the transmission, the Tx beamformer showed in Fig. 16, focuses electronically at different depths and steers the beam by generating properly delayed signals. These delayed signals are summed coherently in the focal point to concentrate the energy in a specific part of the Region Of Interest (ROI). For example, in the case of Fig. 16 the delay to focus each element is:

$$\tau = \frac{r - \sqrt{(x_r - x_n)^2 + z_r^2}}{c} + \tau_0 \quad (34)$$

Where c is the speed of the sound in the medium, p is the probe's element pitch, $X_n = np$, $X_r = \sqrt{(x_r + z_r)^2}$ and τ_0 is the initial delay.

For the spatial impulse response of a single element located at position $X_n = np$:

$$h_x(u, r, t) = h_{0x} X_n \left(\frac{c}{X_n u}\right) \prod \left(\frac{t}{X_n u / c}\right) \quad (35)$$

The transmit spatial impulse response for an element with focusing is:

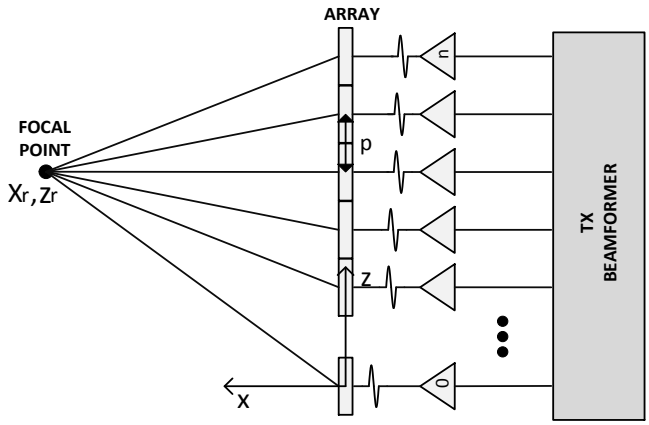

Fig. 16: Tx beamformer.

$$h_n\left(t-\frac{1}{c}\sqrt{(x-x_n)^2+z^2}-\tau\right) \quad (36)$$

The overall array response is simply the sum of the response of each element:

$$h_a(t)=\sum_{-nL}^{nl} h_n\left(t-\frac{1}{c}\sqrt{(x-x_n)^2+z^2}-\tau\right) \quad (37)$$

The pressure can be found from the convolution of the excitation pulse and array response.

The voltage output, including focusing on transmit and receive, can be described by the product of electrical excitation E_{RT}, the array transmits H_T and receive H_R spatial responses:

$$V_0(r,f,\theta)=H_T(r_T,f,\theta_T)H_R(r_R,f,\theta_R)E_{RT}(f) \quad (38)$$

The formulation in the time domain is:

$$v(z,r,t)=h_T * h_R * e_{RT} \quad (39)$$

The modification of the voltage applied at each element by a weighting function is called apodization. It reduces the levels of the side lobes and consequently the echoes due to these lobes mapped into the main beam that causing artifacts. On the other hand, the apodization produces a broadening of the main lobe that decreases the lateral resolution, that is the ability to distinguish between two reflectors situated side by side in the direction perpendicular to the ultrasound beam. Therefore, a trade-off between reduction of side lobes and width of the main lobe is needed. The apodization can be also applied in reception by changing dynamically the signal amplification of each element to control side lobe characteristics.

2.4. Ultrasound Imaging

Ultrasound imaging uses high-frequency sound waves to investigate human body and displays on the screen in different way tissues and organs boundary or blood flow. These methods can be used in industrial environment in order to control the production process and the quality of the products [1].

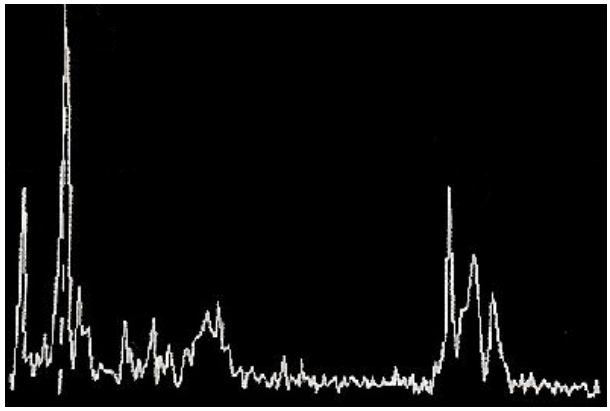

Fig. 17: A-mode image

2.4.1. A-mode, M-Mode and B-mode Images

Pulsed-Echo ultrasound systems have different modality to display images on the screen. The oldest one is the Amplitude mode or A-mode. The system generates a single pulse of ultrasound and send this into the medium through a transducer, the backscattered echoes from different target objects and boundaries are received and amplified. Consequently, a simple one-dimensional ultrasound image is generated as a series of vertical peaks versus time. This mode provides little information on the spatial relationships of the imaged structures. Fig. 17 show an example of the A-mode image.

The Motion mode or M-mode is 2-D image that represents movement of structures over time. The single sound beam is transmitted and the reflected echoes along this line are displayed as dots of varying intensities thus creating lines across the screen. The measures are repeated to produce adjacent lines which show how the

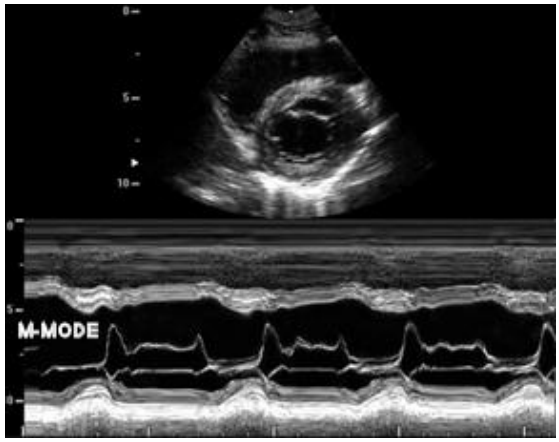

Fig. 18: Mitral valve, on the top the B-mode on the bottom the M-mode image

Fig. 19: B-mode image

structures intersected by that line move toward or away from the probe over time. Fig. 18 shows an M-Mode image of a mitral valve.

The Brightness mode or B-Mode image is a two-dimensional cross-sectional image that represent tissues and organs boundaries inside the body composed of bright dots representing the ultrasound echoes. It is constructed from echoes, which are generated by reflection of ultrasound waves at tissue boundaries, and scattering from small irregularities within body. The brightness of the image at each point is related to the amplitude of the echo, giving rise to the term B-mode. These images allow for visualization and quantification of anatomical structures, as well as for the visualization of diagnostic and therapeutic procedures. In Fig. 19 there is an example of B-mode image.

2.4.2. Ultrasound Velocity Profile (UVP)

The Ultrasound Velocity Profile (UVP) technique assesses the velocity profile of a fluid in a pipe, this technique is used in biomedical applications to obtain the velocity profile of the blood which flows in the vessels or in industrial applications to evaluate the velocity profile of the opaque fluids that flow in a tube.

The principle to obtain the velocity profile is based on ultrasonic echography and Doppler effect. An Ultrasound transducer transmits a burst into the medium. When the burst encounters moving particles, an echo with a frequency shift directly related to the particle axial velocity is produced, according to the Doppler effect. By measuring the frequency shift at hundreds of depths aligned along the axis of the emitted beam the velocity profile along this axis can be obtained. Fig. 20 shows a typical velocity profile of the opaque fluid in a pipe.

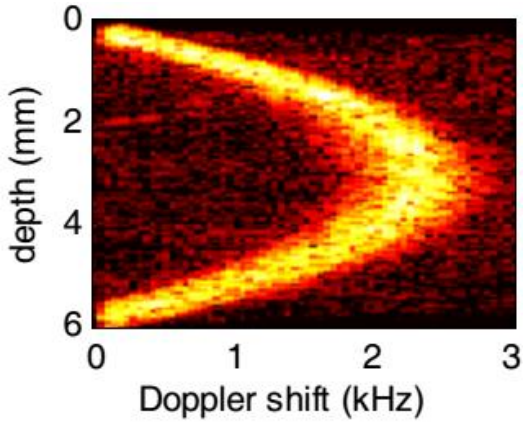

Fig. 20: Velocity Profile of the fluid in a pipe obtained by ultrasound system

2.5. Pulse Wave Ultrasound Systems

The Pulse Wave Ultrasound System (PWUS) is showed in Fig. 21, every Pulse Repetition Interval (PRI), it transmits the excitation signal by a probe, then switches in Rx mode to acquire by the same probe the backscattered echoes; the sample frequency is in a range between 40-100 MHz. Probes operating frequencies are in the 1-40 MHz range. Higher frequencies are in principal more desirable since they provide higher resolution, but medium attenuation limits the penetration distance of the waves at high frequency. The PWUS is made up of an analog Tx and Rx sections both connected to a probe as well as to a control unit, that manage every operation needed to obtain the results. During the transmission, the system generates the excitation signal transmitted by a probe which propagates in the medium and produces echoes when encounters scatters or impedance discontinuities. The echoes propagate back to the probe, producing a low voltage signals which is managed by the Rx section that amplifies and converts to digital

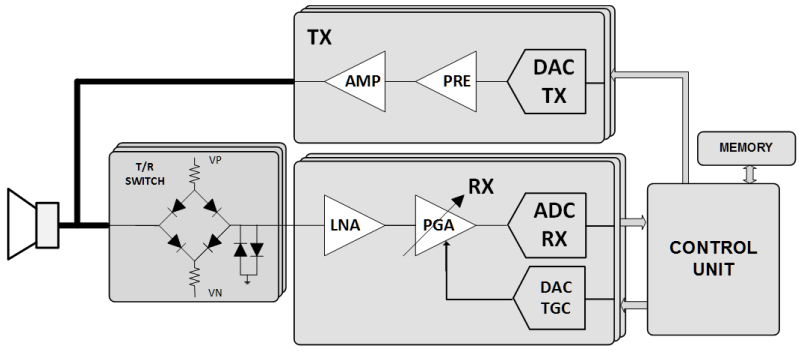

Fig. 21:Block scheme of Ultrasound Pulse Wave System.

the signals. The processing operations are typically performed by Field Programmable Gate Arrays (FPGAs) and Digital Signal Processors (DSPs); the choice depends of the system complexity. Nowadays the ultrasound systems are largely based on digital devices and only the restricted area called Analog-Front-End (AFE), directly connected to the probe uses analog devices.

2.5.1. Tx Section

For each transducer, the Tx section is composed by a Digital to Analog Converter (DAC), a preamplifier and a high voltage amplifier, used to increase the amplitude of the signal up to $\pm$ 100V.The DAC controls the Tx section in order to shape the transmit pulses for better energy delivery to the transducer elements. The Tx signals go through a transmit/receive (Tx/Rx) switch, which prevent the high voltage signals coming from Tx section damaging the Rx section, able to manage signals with amplitude up to $\pm$ 100mV. A T/R switch includes bridge of biased diodes used to clamp the signal with amplitude over the diode threshold; otherwise, the signals under the threshold (e.g. Rx signal) pass through the bridge and arrive to the Rx section. The Tx/Rx switch must have fast recovery times to ensure that the receiver gets on immediately after a transmitted pulse.

2.5.2. Rx Section

For each transducer of the probe the Rx section is made up of a chain composed of Analog to digital converter (ADC) and amplifiers. The Low Noise Amplifier (LNA) is the most important devices because determine the noise performance of the system. To handle small-backscattered signals it must have an excellent noise performance in the bandwidth of the system to introduce a very low amount of noise and distortion to guarantee high SNR ratio.

The second amplifier is a Programmable Gain Amplifier (PGA), which has the purpose of the Time Gain Amplifier (TGC)When the ultrasound signals propagate in the medium, it suffers an attenuation directly related to the signals roundtrip, thus the echoes strength decrease with the time (e.g. it has travel more). The gain of the TGC is typically a ramp as a function of time to adapt the backscattered signals amplitude to the dynamics of the ADCs. Finally, the ADC digitalizes the amplified echoes.

2.5.3. Control Unit

The control unit is the core of the system, embeds the programmable digital devices (e.g. FPGA, DSP), memories and the transceivers needed to transmit the processed data. In a system that manages few transducers, single programmable device is enough to manages every digital device and processing the data.

Otherwise, the architecture can be composed by one or more programmable digital devices, that manage the others digital devices, set the timetable and process the data to obtain the results. Normally, each programmable device has a dedicated fast memory to store data.

At the beginning, the samples of the transmission signal are generated and conveyed to the Tx section to generate the analog excitation signal for every single transducer. In the receive mode the Rx section converts and amplifies backscattered signals and programmable devices process the data to obtain the final results. In the multi-transducers mode, each transducer has a dedicated Rx section to amplify and digitalize the echoes that finally are beamformed and processed to obtain results.

Chapter 3. Ultrasound System for Non-Destructive Tests on Concrete

In this chapter the design of an Ultrasound System used to evaluate the mechanical properties of the concrete is presented. The system is employed for measuring the concrete strength to ensure safe and durable constructions. A brief introduction gives an access to the chemical process needed to produce concrete.

3.1. Introduction to Concrete

Concrete is one of the most widely used material for constructions as bridges, skyscrapers, highway, houses etc.. Evaluating its compressive strength is highly requested to ensure durable and safe constructions. The concrete is composed of cement powder, sand (fine aggregates) and gravel (coarse aggregates). When dissolved in water they produce a chemical reaction called Hydration [3]–[5]. As depicted in Fig. 22, in the first stage the cements powder combines with water, then the hardening process starts.

The Hydration reaction is mostly exothermic, that is, the reaction generates heat and gradually the products bond together to form concrete. The evolution of the heat during the reaction (Fig. 23) gives information about concrete hardening process [6], [7]. Based on the characteristic of the heat curve, the hydration process can be distinguished in five stages; dissolution, dormant, acceleration, deceleration, and steady state. At the stage 1, cement powder dissolves in water and the temperature decreases for a short period; the stage 2 is the dormant period during which almost no reaction occurs, needed to achieve suitable concentration of reagents in solution. At stage 3 the hydration starts and the temperature increases rapidly and reaches its maximum [8] . During the stage 4 the temperature decreases to less than half of its maximum. At the stage 5 hydration keeps going slowly to reach the final strength of the concrete.

The concrete properties depend of aggregates, relative quantities of cement-water and cement strength. In details, they are influenced by:

- Ratio water cerement (w/c);
- Ratio cement aggregates;
- Quantity and size of aggregates;
- Stiffness of aggregates;

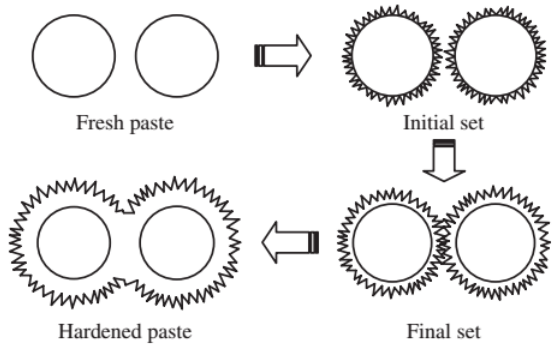

Fig. 22: Hydration steps. At the beginning the cement powder reacts with water and then aggregates bond together to form concrete.

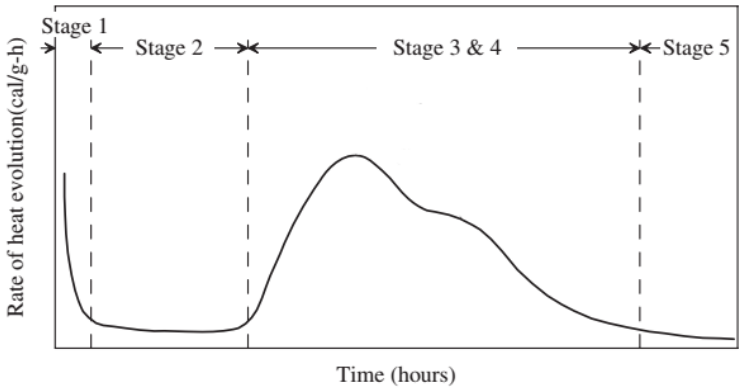

Fig. 23: Temperature evolution during Hydration process.

- Air in concrete.

Water in the hydration process [9]–[11] can be distinguished in four kinds according to the role: chemically reacted water (needed for the reaction), absorbed water, water entrapped in the layer of the concrete, and free water spread outside of the fresh concrete which creates capillary pores and influences the permeability of concrete.

The Aggregates reacts with cement paste and contributes on stiffness and strength of the concrete in function of theirs shape, dimension, material and quantity.

Air bubbles are created during mixing process and survive to concrete hardening. The primary purpose of these, is to increase the durability of the hardened concrete, since they relieve the internal pressure by providing tiny chambers, which allow water expansion when it freezes. The secondary purpose is to increase workability of the concrete while in a plastic state.

3.2. Concrete Compressive Strength Evaluation

Compressive Strength is defined as the ability of a material to resist the stress generated by an external force without failure. Failures are frequently identified with the appearance of cracks. Compressive Strength is measured by applying a force on the faces of a concrete cube and can be expressed as σ [3] :

$$\sigma = \frac{F}{L^2} \qquad (40)$$

Where F is the applied force on the square of the concrete cube of side L. The dimension used to measure σ is MPa:

Fig. 24: Pouring fresh concrete inside the mold.

3.2.1. Classical Methods for Compressive Strength Evaluation

The most used tests are mechanical: First of all fresh concrete is poured inside the cube molds (Fig. 24)[3], [12]. After 28 days, the hardening process can be considered in steady state and the concrete cubes are removed and cleaned. As reported in Fig. 25, the cleaned specimens are placed under a calibrate compression machine that crashes them and measures the applied force on the surface, that is the compressive strength.

Penetrometer obtains the strength by measuring the force required to penetrate the surface of concrete for 15 mm using a needle (Fig. 26), whereas Hilti needle uses a gun to drive a stud inside the concrete to obtain the strength by measuring the penetration depth (Fig. 27) [12], [13].

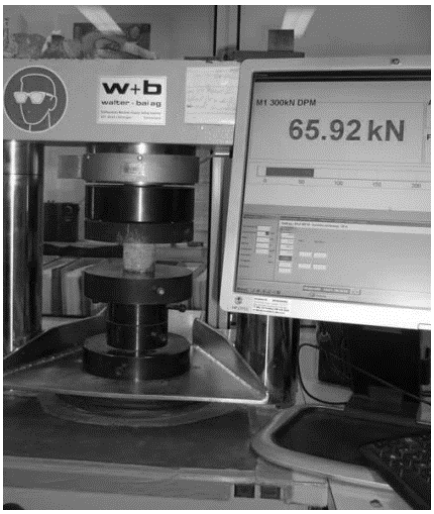

Fig. 25: Cleaned Concrete Sample, inside the Compression Machine.

Fig. 26: Concrete Strength measurement by Penetrometer

All these mechanical approaches are manual, time consuming and crush the samples to determine the concrete strength. Moreover, measuring the concrete strength at the steady state don't give info about the strength evolution during the hydration process.

Another approach, typically used in labs, assesses concrete strength by measuring the cumulative heat release per unit of volume of mixed water [8]. It's a linear relationship (Fig. 28) that has been validated for a wide variety of concrete mixtures at ages from 1 d to 28 days [6] and can be evaluated by using an isothermal calorimetry, which logs the temperature history of the fresh concrete poured into a calibrated isolated container. In Fig. 29 is showed a calorimetry with 8 cells, that uses PT-100 sensors to measure the temperature and records the temperature history of the samples.

Another method is based on measuring the changes in electrical resistance defined as [3], [14]:

$$R = \rho \frac{L}{A} \qquad (41)$$

Where R is the resistance, ρ the resistivity, L the length and A the cross-sectional area of the sample. The changes of the concrete resistivity are related to the evaporable water content in concrete, which varies with water/cement ratio (w/c), degree of hydration, degree of saturation and ion concentration in water.

Fig. 27: Concrete Strength measurement by Hilti Needle

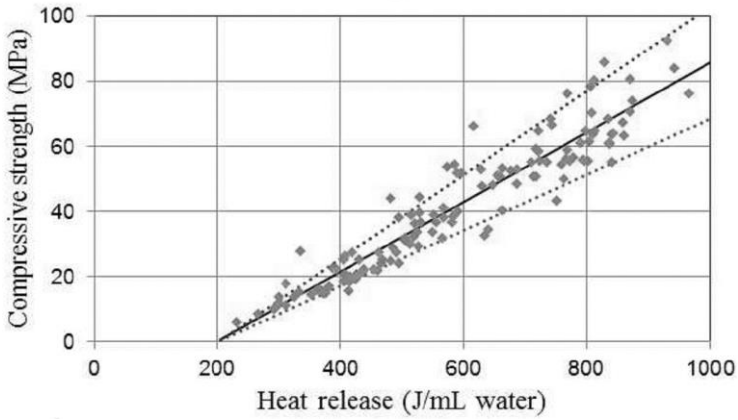

Fig. 28: Compressive Strength vs Heat release per mL of water. The solid line indicates the best fit linear relationship

A system, used to measure the concrete resistivity, typically used in labs, is depicted in Fig. 30. The circuit is made up of a primary coil with wound wires and a concrete circular sample that acts as the secondary coil of the transformer.
If an AC current is applied to the primary coil, on the circular sample a current is present due to the mutual induction. By measuring the inducted current, the curve of resistivity versus time can be obtained. Another approach consisting of four equally spaced point electrodes inserted onto the concrete surface, as illustrated in Fig. 31. The two outer electrodes induce a sinusoidal current, typically with a frequency between 50 and 1000 Hz and the two inner electrodes measure the resulting potential difference. The resistance R is the ratio of the voltage and the current and can be converted to resistivity ρ by relation:

Fig. 29: 8 chambers Calorimetry

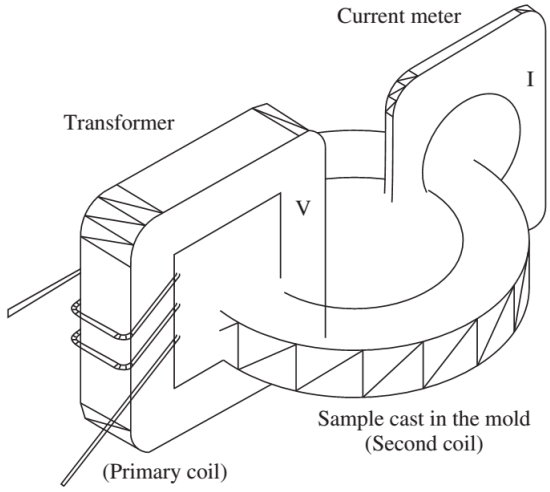

Fig. 30: Electrical resistivity setup

$$\rho = 2\pi aR \qquad (42)$$

Where a is the electrode spacing. By the resistivity curve, the hydration characteristics and consequently the concrete compressive strength is obtained. Good electrical contact between electrodes and specimen is mandatory to obtain accurate measurements, so the electrodes must be placed by trained operators and frequently checked. In Fig. 32 is showed an example of relationship between concrete strength and resistivity.

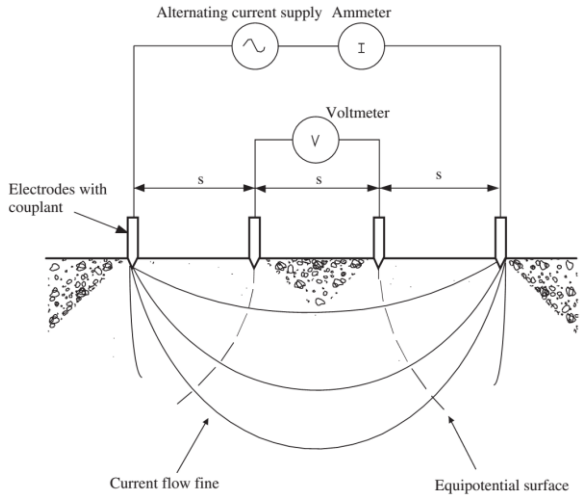

Fig. 31: Four electrode electrical resistivity setup

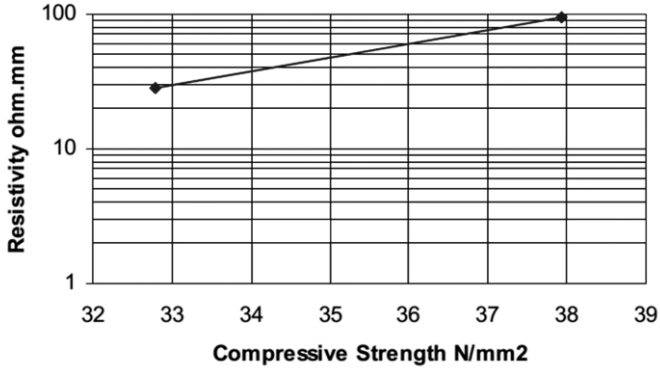

Fig. 32: Concrete Strength vs Resistivity

3.2.2. Ultrasound Methods

In this chapter nondestructive methods based on the propagation of the Ultrasound waves inside the concrete are described [15]–[19].

The velocity of the ultrasound waves in the concrete is strictly related to the hydration process, and therefore, to the concrete strength [20], [21]. Two transducers placed at distance (d) on the sample, are used to measure the time (Time of Flight) needed by the wave to cover this distance. One transducer transmits a wave inside the concrete, the other receives the attenuated signal after the Time of Flight (TF). The velocity v is achieved by:

$$v = d/TF \tag{43}$$

To perform the measurements by longitudinal waves an access to opposite surfaces, where to place transducers (Fig. 33) is needed. Since the opposite surfaces are not always easily accessible, surface waves can be used, which requires only an access to one surface of the sample, see Fig. 34. These methods, where ultrasound waves travel inside the concrete, are highly influenced by

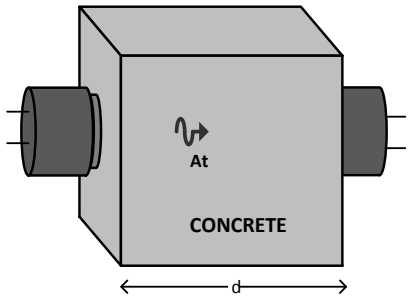

Fig. 33: Time of Flight measurement. Compression waves

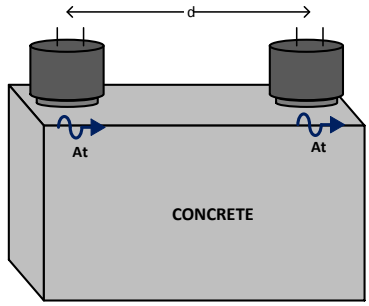

Fig. 34: Time of Flight measurement. Surface Waves.

concrete heterogeneities and the presence of reinforced steel which produces multi-scattering and degrades the quality of the measures.

The proposed system is based on the Ultrasound Pulse Echo Reflectometry (UPER) technique [6], [22]–[24], that uses wave reflection at the interface between concrete and a wave guide to assess the shear wave reflection coefficient, needed to measure the shear modulus G, and therefore the compressive strength σ, which is proportional to G^n [25], [26].

Shear waves are preferred to longitudinal waves for evaluating the concrete compression strength, since their propagation speed is more sensitive to the concrete hardening process [27].

To evaluate the properties of the specimens an ultrasound shear transducer and Plexiglas wave guide are used. Plexiglas because well matched with the concrete, is cheap and easy to clean. In a first stage of the measurement process, the amplitude of the transmitted wave A_i is measured by firing ultrasound bursts inside the wave guide in contact with air (without concrete). The amplitude of the reflected wave at the interface is obtained as depicted in Fig. 35. Since the acoustic impedance of the Plexiglas Z_1 is much higher than the acoustic impedance of the

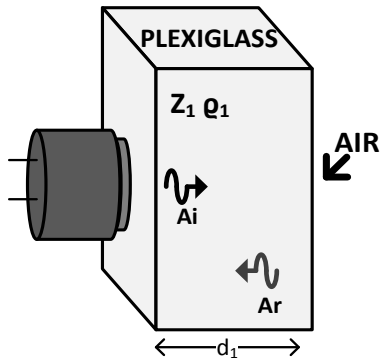

Fig. 35: Transmitted and reflected waves in the Plexiglas coupled with air.

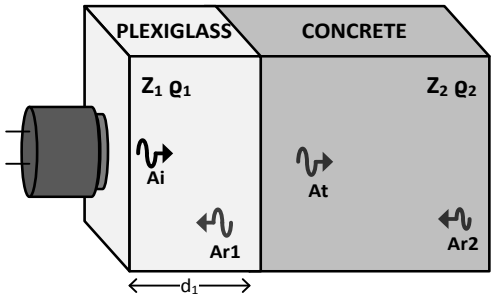

Fig. 36: Incident, transmitted and reflected waves when the sample is coupled with a wave guide.

air Z_a, the reflection coefficient is $r_{1a} = \frac{Z_a - Z_1}{Z_a + Z_1} \approx -1$, so, the amplitude of the receive wave A_r can be considered the amplitude of the transmitted wave A_i, used as reference to obtain the reflection coefficient r_{21} between concrete and wave guide :

$$r_{21} = \frac{A_{r1}}{A_i} \qquad (44)$$

A_{r1} is measured by coupling the concrete sample with Plexiglas (Fig. 36) and transmitting a new short burst through the wave guide. Once the transmitted signal reaches the interface, it is partially reflected (A_{r1}) and partially transmitted in concrete (A_t). The reflected wave (A_{r1}) is received back by the transducer and acquired together with the time of flight t_{f1}needed to obtain the acoustical impedance of the Plexiglas:

$$Z_1 = \rho_1 v_1 = \frac{\rho_1}{t_{f1}} d_1 \qquad (45)$$

where ρ_1 is the density of the Plexiglas and d_1 the length of the wave guide. The Shear modulus of the concrete G_2 and the Young modulus E_2 are obtained by the following relation:

$$G_2 = \rho_2 v_2^2 = \rho_2 \frac{Z_2^2}{\rho_2^2} = \frac{Z_2^2}{\rho_2} = \frac{Z_1^2}{\rho_2} (\frac{1 - r_{21}}{1 + r_{21}})^2 \qquad (46)$$

$$E_2 = 2G_2(1 + v_2) == 2\frac{Z_1^2}{\rho_2} (\frac{1 - r_{21}}{1 + r_{21}})^2 (1 + v_2) \qquad (47)$$

Where v_2 is the Poisson ratio, Z_2 and ρ_2 are the acoustical impedance and the density of the of the sample. Finally, the compressive strength σ_2 can be achieved by [28]:

$$\sigma_2 = \left(\frac{49000}{E_2}\right)^2 \qquad (48)$$

The transmitted signal frequency is crucial to obtain accurate measures, since, the relation (48) is valid when the wave length λ_2 is larger than the biggest sample particle. Only in this case the sample can be considered homogeneous or transparent to the wave. The size of the biggest particle of cement paste is around (< 100 μm), so, the cement can be considered transparent at the frequency of 1 MHz ($\lambda_2 = v_2/f = 1000\frac{m}{s} \cdot 1MHz = 1mm$). However, in the concrete with aggregates larger than 1 mm the multi scattering occurs and influences the measures.

3.3. The UPER System

The presented electronic system is based on UPER technique. It manages up to 8 transducers that are typically distributed on the bottom of a Plexiglas cell of 5cm diameter, where the concrete is poured just after its preparation. For each transducer, the measuring procedure detailed in the second part of 3.2.2 is performed and hundreds of echoes are accumulated to improve the noise performance.

The reflection coefficient is calculated by comparing the accumulated signal to the echo measured in condition of total reflection (e.g. at Plexiglas/air interface). The measurement is repeated in the position covered by the several transducers to compensate for the non-homogeneous aggregates present in the cement. The system can be powered by battery and deployed in the construction site to automatically monitor the hydration process for days, by using a connection to a host via Wi-Fi.

3.3.1. Hardware Architecture

The UPER system is composed of two boards, the UPER main board (UPER-MB) and the commercial microprocessor board Z48-C1 (Schmid Elektronik AG, Munchwilen, Switzerland), which is installed on the bottom of the UPER-MB.

The basic blocks of the system are reported in Fig. 37, while the main features are listed in TABLE I. The core of the UPER-MB is a Field Gate Programmable Array (FPGA) of the Cyclone III family (Altera, San Jose, CA), which manages the measuring process, controls the ultrasound front-end and communicates to Z48-C1 module. The FPGA includes an arbitrary waveform generator (AWG) that synthetizes the transmission burst with a programmable number of cycles and

TABLE I: UPER-SYSTEM MAIN FEATURES

Features	***Value***
Dimensions	15x9 cm
Supply Voltage	10-30 Vcc Li-ION battery/Power Supply
Power	3 W max; 50mW in power-down
Non-Volatile Memory	µSD up to 64MB
Tx/Rx Channels	8 Multiplexed
Tx/Rx Frequency	0.7-5 MHz
Tx Voltage	6 Vpp
Tx Waveform	Programmable Arbitrary Waveform
Sampling Frequency	75 Msps
Input Gain	5-55 dB
Input Noise	2 $\boldsymbol{nV/\sqrt{Hz}}$
Programmable Parameters	Gain, PRI, Tx Pulse, Rx Echoes to average, Switch On-time

frequency in the range 0.7-5 MHz weighted through a Tukey window. Moreover, the FPGA integrates the low-level interfaces used to communicate with all the devices present on-board, like the high-speed Analog-to-Digital (AD) converter that samples the received echoes at 14-bit 75Msps, the Digital-to-Analog (DA) converter for generating the TX pulse, the DA converter that generates the analog signal for setting the input gain of the ultrasound front-end, the System Management Bus (SMBus) interface for the smart battery, etc. The FPGA integrates a command interface used to receive commands from the processor board and a data interface to download the measurements

The measurement operation starts when the AWG in the FPGA synthetizes the samples of the TX pulse. The samples are DA converted at 75Msps, amplified (TX AMP) and applied to the output multiplexer (SW-MUX). The multiplexer, set by the FPGA, connects the ultrasound section to one of the eight different transducers wired to the board (see SMA connectors on the right of the board in Fig. 38). The weak echoes received are amplified by a chain composed of Low Noise Amplifier (LNA) and Programmable Gain Amplifier (PGA) and converted at 75Msps by the Rx AD converter. The FPGA, stores in memory the acquired samples, thus, at the end of measure cycle they are downloaded by the microprocessor board (Schmidt Z48-C).

The Z48-C1 is a mixed signal core module based on the 525MHz ADSP-BF548 processor (Analog Devices Inc, Norwood, MA), provided of 8-high impedance analog inputs with overvoltage protection which allow direct connection to external signals without any external circuitry.

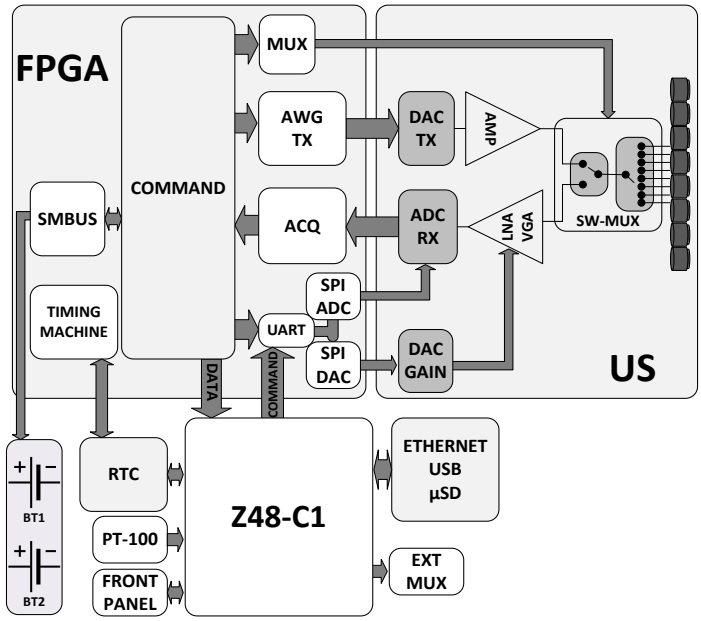

Fig. 37: Block scheme of UPER system

The main features are reported in TABLE II. In the UPER system, the Z48-C1 module interfaces to two PT-100 sensors employed for measuring the temperature of the concrete. The module is connected to a Real Time Clock (RTC), useful to manage alarms at programmable times, and a simple control panel. All measurements (temperatures and ultrasound data) can be stored in the local µSD or sent to host for high level processing by a 100 Mbit Ethernet, Wi-Fi or USB connection. The module can be programmed through the popular high-level language LabView (National Instruments, Austin, TX), which greatly simplifies the final industrial application.

The power section is made up of switching and linear regulators that supply every device on the UPER system. It can be connected to a 10-30V industrial power unit (nominal 24V) or to a Li-ION smart battery.

The system includes the smart battery charger LTC4100 (Linear Technology Corp., Milpitas, CA), that charges the battery when the system is connected to the line. Batteries, charger and the system share status and charge parameters through the SMBus.

The RTC is always powered and controls the main power switch, so that it can power the full system when an alarm occurs. Fig. 38 shows the UPER system powered by the Li-ION battery ND2034 (Inspired Energy, Newberry, FL) and

Fig. 38: UPER-MB with Z48-C1

Fig. 39 depicts components placement on the UPER-MB with the FPGA and the Z48-C1.

The Printed Circuit Board (PCB) is composed by 8 layers used to better isolate sources of noise. Copper shields can be placed on the Rx section and on the ultrasound switching power supply section located on the bottom of the UPER-MB, for improving the ability of Rx section to operate without interfering with other devices and keep the echo signal as clean as possible.

TABLE II: Z48-C1 MAIN FEATURES

Features	***Value***
Flash on Board	256 MB
Analog In.	8 industrial range 16 bit 200KHz
DIO	Up to 74 multiplexed with other functions
Timer In.	Up to 7
Serial Interfaces	3x UART, 2xTWI, 1xSPI
Interfaces	Ethernet, USB, SD card
Counters	Up to 6
Communication	Ethernet 100Mbit, USB 1.0
Supply	3.3V
Dimension	6.6 x 5.3 cm

3.3.2. FPGA Firmware

As showed in Fig. 37, the FPGA operations sequence are managed by a TIMING MACHINE that allocates time slots for every FPGA operation. By an UART port the Z48-C1 sends configuration parameters to the COMMAND block, that produces commands needed to every operation of the system. The measurement operation starts when the FPGA produces the samples of the transmission pulse, which is applied to the output multiplexer (SW-MUX).

The multiplexer, set by the FPGA, connects the ultrasound section to one of the eight different transducers connected to the board. In reception, the received weak echoes are amplified, acquired and stored in the memory. The FPGA repeats the described procedure a programmable number of times (tens to hundreds) and accumulates in memory the samples. This strategy is used on the stationary target for improving the signal-to-noise ratio of the acquired echoes. Finally, the amplitude is calculated and the result is moved to the microprocessor module by a parallel interface, which finalizes the calculations.

The SMBUS block manages the communication between smart batteries, smart charger and FPGA, to collect information about the status of the battery and the charger and share this information to the microcontroller board. SPIs are used to set the parameters of the AD and DA converters used to set the gain of PGA amplifier.

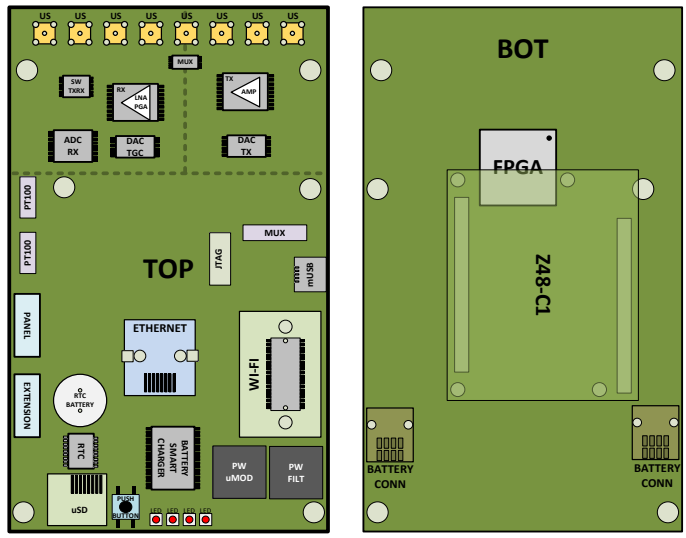

Fig. 39:UPER-MB system boards block scheme

3.3.3. Sequence of operations

In the typical operation sequence the system is normally in power-down mode, to save power. A RTC or a push button on the user panel commands the wake-up of the system. The microprocessor module sets the parameters in the FPGA and commands the starts of the measurement cycle. As soon as the results are ready, they are moved to the microprocessor module that stores them in the SD-card and/or sent them by WiFi or Ethernet to a host. The processor programs the RTC for the next measurement and switch the system in power-down to close the cycle.

3.4. Tests and Results

In this chapter tests and measurements are reported. In the beginning, measurements on the metal disc and the Electro Magnetic Interference (EMI) of the system is evaluated to understand the functionality and performance of the electronics. Finally, tests on the concrete are reported for different mixtures.

3.4.1. Measurements on Metal Disc

The preliminary tests on the UPER-MB are performed by connecting the transducer Panametrics V103 (Panametrics-Olympus NDT Inc. Waltham, Massachusetts, USA) on the metal disc with diameter of 10 cm and thickness of 1 cm. In Fig. 40 are reported the transmission burst composed of 6 sinusoidal cycles tapered with a Hann window and the echoes signals originate at the first

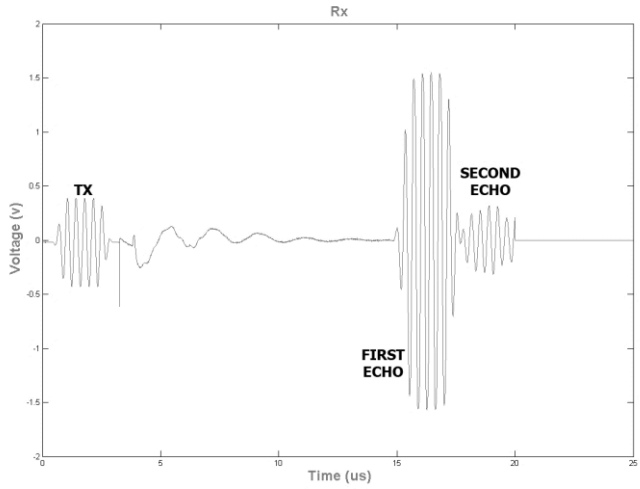

Fig. 40: UEPER-MB test on metal disc.

Fig. 41: Anechoic chamber Setup

interface (transducer-metal) and second interface (metal-air) amplified of 20dB both.

3.4.2. Electro Magnetic Interference

To evaluate the EMI of the UPER system some measurements in an anechoic chamber are performed. Fig. 41 depicted the anechoic chamber whit the system placed at 10 m from the antenna.

Fig. 42 reported the radiated emissions of the UPER. The system is compliant to EN55011 [29] (Industrial, scientific and medical appliances) since, the value of the electric filed generated is under the limits dictated by the regulation in a bandwidth from 30 MHz to 1GHz.

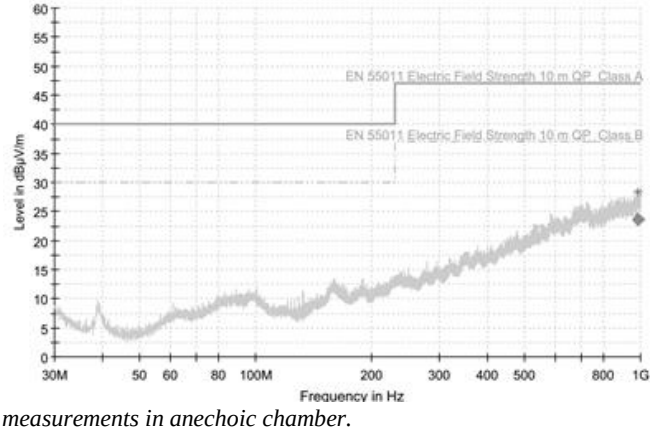

Fig. 42: EMI measurements in anechoic chamber.

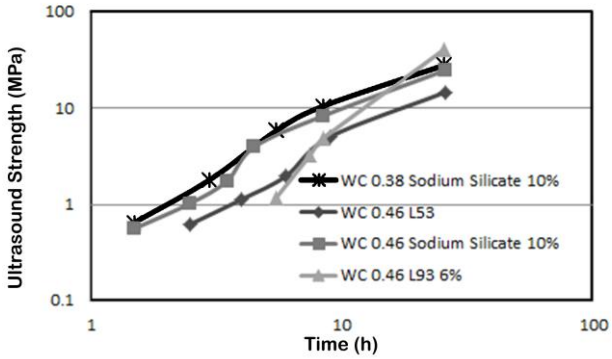

Fig. 43: Evolution of the strength as function of the time for 4 different cement paste, measured by UPER system

3.4.3. Measurements on Cement Paste

In Fig. 43 is reported the evolution of the strength as a function of the time measured by the UPER system for the pure cement pastes (Cement paste without aggregates) in 4 different mixtures.

The comparison of the concrete strength measured with ultrasound and with mechanical technique is depicted in Fig. 44. The correlation is in the range of ± 20 % over more than 2 orders of magnitude of strength evolution over the first days. A coefficient of variation of 10% of the compression tests made on a series of 10 probes has been obtained. For the ultrasound, a variation from 20% for the lower strength (<2MPa), 15% for the strength ranging from 2-20MPa and 10% for higher has been obtained on a series of 7 tests.

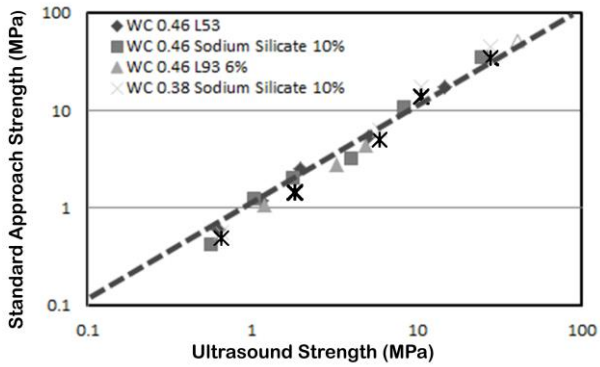

Fig. 44: Comparison of standard approach and Ultrasound measurements for 4 different cement pastes. Dashed line represents the perfect correlation.

3.4.4. Measurements on Concrete

In Fig. 45 ultrasound measurements performed on the interface between wave guide and concrete with different percentage of round and crushed aggregates are reported. The concrete with aggregates less than 1 mm gives a perfect correlation between compression and ultrasound measures. On the other hand, the measurements performed on the concrete with aggregates larger than 1 mm are less accurate. The correlation is good for all concentrations except for the high content of aggregates (70 %) where a difference of a factor of 1.6 to 1.8 is achieved. The difference is more pronounced for the rounded aggregates respect of crushed.

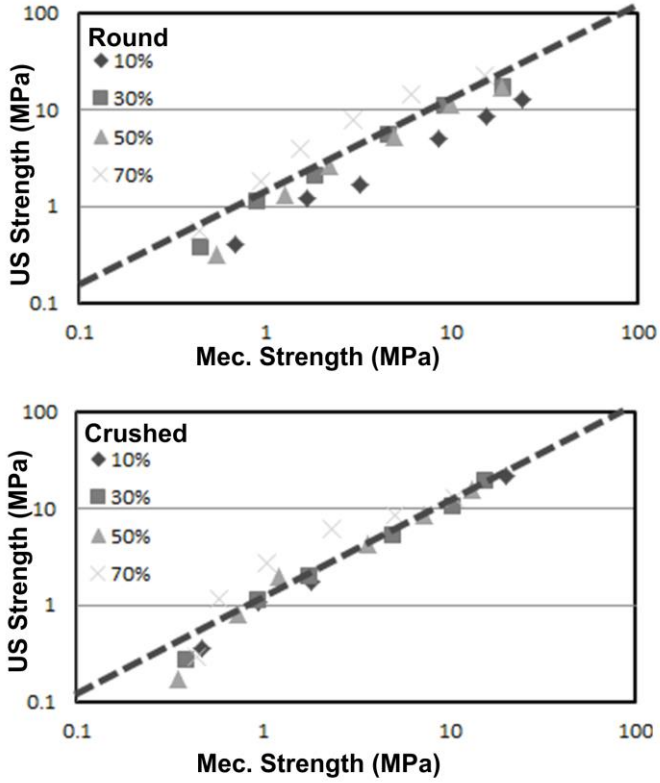

Fig. 45: Correlation between the strength measured with compressive test and ultrasound system on the concrete with different concentrations of round and crushes aggregates.

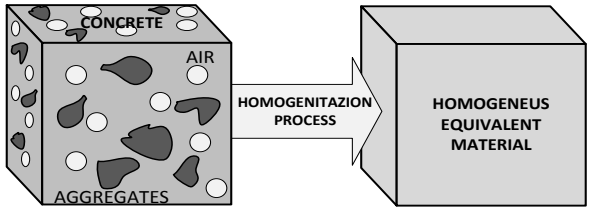

Fig. 46: Homogenization process for a concrete cube.

The ultrasound technique measures the evolution of the paste without considering the effects of the aggregates and air voids, so, to estimate the concrete strength when the aggregates are larger than 1mm or in high percentage a method that transforms concrete in a homogeneous material, with the same dimensions and macroscopic strength is needed (Fig. 46) [30], [31].

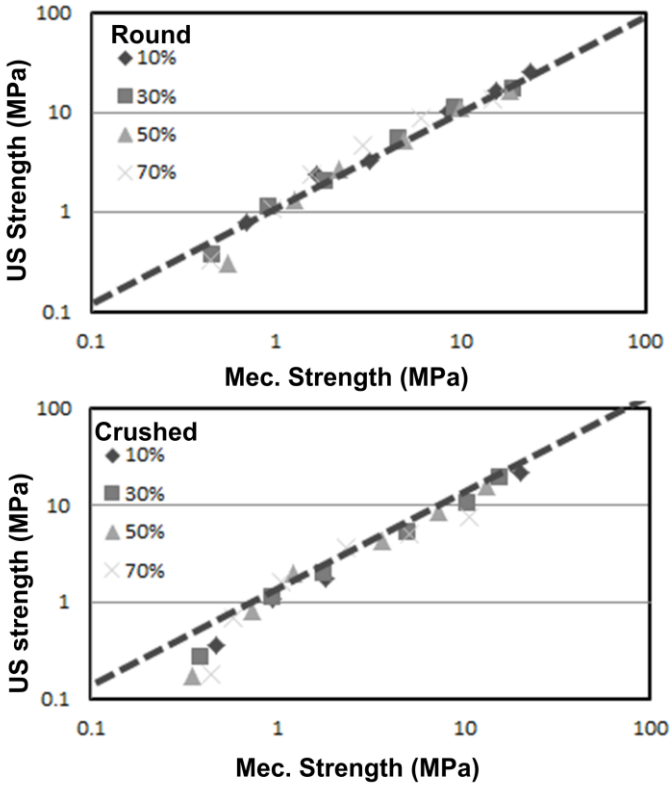

Fig. 47: Correlation between the strength measured with compressive test and ultrasound system on the concrete with different concentrations of round and crushes aggregates. Homogenization process is applied by a parameter.

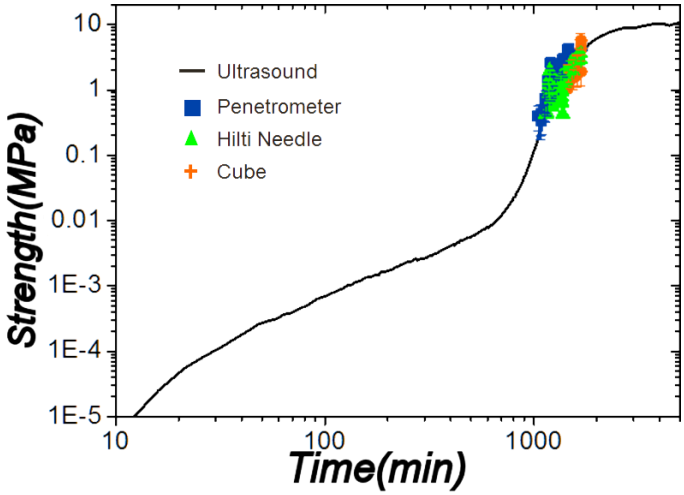

Fig. 48: Comparison between measurements performed by classical mechanical methods and ultrasound method.

This method called Homogenization, processes ultrasound data considering quantity, characteristics and affinity of cement paste and aggregates to estimate the strength of concrete. Since, the parameters of the aggregates are difficult to access, the homogenization consists of a comparison between evolution of strengths measured on the cubes with and without aggregates to back calculate the concrete strength from paste strength.

The concrete strength evolution is measured with mechanical methods and the measures on the cement paste is performed by ultrasound method.

Fig. 47 showed the measurements of the concrete strength where the correction obtained by the homogenization process has been considered, currently, is a simple multiplicative factor (0.6), that shifts the curves obtained with ultrasound measurements. As shown in the graphics (Fig. 47), this simple correction obtained by homogenization process improves the results obtained with ultrasound.

3.5. Discussion and Conclusion

The UPER system is capable to measure the entire evolution of the concrete strength during hardening process by using reflectometry technique. Other systems, currently used to measure the concrete strength are totally mechanical and measure the strength in a limited interval, as depicted in Fig. 48.

The UPER system embeds all the electronics needed to manage up to 8 ultrasound transducers in a compact size (15 x 9 cm). During an ultrasound measurement cycle hundreds of measurements are accumulated to improve noise

performance. Thanks to the programmable architecture, managed by FPGA and the Z48-C1, the acquisition strategies are programmable and data can be stored and/or transmitted to host by 100Mb Ethernet, Wi-Fi, USB or stored in uSD card. Rx chain composed by LNA and PGA limits the input noise level and sets the gain to accommodate echo signals in a wide dynamic range. The measurements are well correlated to those obtained by the reference methods except for the concrete with high content of aggregates where multi-scattering occurs and a correction coefficient obtained by homogenization process must be used to improve the measurements accuracy. These features, joined to the capacity to autonomously run by batteries for days, allow the installation of the system on-site.

3.6. Contributions on Concrete Strength Evaluation

This activity produced two papers presented at an international and a national conference.

The proceedings, reported below, describe the Ultrasound System and the method used to measure the concrete strength. A comparison of results obtained by classical and ultrasound method are reported.

1. **Meacci, V.**, Ricci, S., Bruehwiler, A., Lootens, D.: Compact ultrasound board for measurement of concrete compressive strength. 2016 IEEE International Ultrasonics Symposium (IUS) Proceedings, pp. 1-4 (2016).

2. **Meacci, V.**, Ricci, S., Bruehwiler, A., Lootens, D.: Non Destructive Ultrasound Equipment to Evaluate the Concrete Compressive Strength. Applications in Electronics Pervading Industry, Environment and Society. (In press).

All contributions are reported in section 1.2.

Chapter 4. **Industrial Fluids Characterization**

In this chapter an Ultrasound System used to characterize industrial fluids is presented. The system is employed for measuring the rheological properties of fluids involved in the production of food, medicines, cosmetics etc. It allows controlling the production chain and guarantee the products quality. A brief introduction gives an access to the rheological properties of fluids.

4.1. Fluids Rheology Basics

The assessment of the fluids properties in chemical, cosmetic, pharmaceutical, and food industries is fundamental for optimizing the production process. Moreover, their careful monitoring during the production steps guarantees the final product quality [32].

The science that studies the deformation and flow of the fluids or suspensions is called Rheology [33]. It can be defined as the study of the viscous characteristics of the suspensions, and more precisely as the relationship between shear stress and shear rate (Fig. 52), measured by a viscometer and presented in a plot named rheogram.

To understand the behavior of the fluid or suspension and consequently the shear stress and shear rate, the model of two plates with the fluid in-between can be used (Fig. 49). The shear stress τ is defined as the force F applied to the upper plate divided by the area of the plate A (Fig. 50). To obtain the shear rate, the velocity v of the upper plate, is divided by the distance h between the two plates (Fig. 51). The relation between shear stress and shear rate (Fig. 52) provides crucial information as Yield stress and Viscosity.

Yield stress is the finite stress that should be applied before fluids begin to flow in laminar, turbulent or transitional regimes. In laminar flow, the motion of the particles is in straight lines parallel to the pipe walls. Turbulence is a form of fluid motion which is characterized by irregular, random movement of fluid, both parallel and transverse to the direction of the main flow. The transition region is expressed as a region between laminar and turbulence flow.

Viscosity is the measure of a fluid's internal resistance to being deformed.

For a Newtonian fluid, the shear stress is equal to the product of the shear rate $\dot{\gamma}$ and the viscosity η.

$$\tau = \dot{\gamma} \cdot \eta \qquad (49)$$

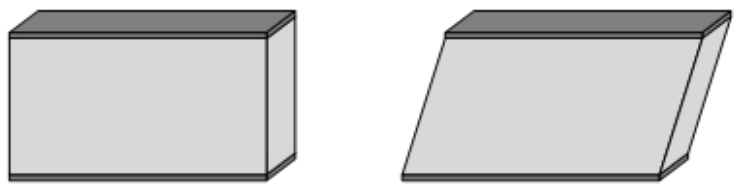

Fig. 49: Two plates model of the fluid.

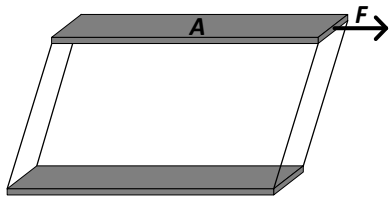

Fig. 50: Two plate Models, Shear stress.

For a non-Newtonian fluid, the relationship between the shear stress and shear rate is non-linear and the viscosity at certain temperature and pressure depends of shear rate and flow geometry [34].

4.2. Rheology Parameters assessment

In first part of this chapter a selection of the most used, mechanical methods used to assess rheological parameters of the fluids in the lab are presented. In the second part a method capable to assess the rheological parameters of fluid by measuring the radial velocity distribution of the fluid through a non-invasive Doppler technique, employed also in biomedical investigations [35] is described.

4.2.1. Classical Methods

Classical approaches used in laboratory to establish the relation between the shear stress and shear rate of a specific fluid, are rotational, capillary and tube viscometer [33], [36].

The rotational viscometer measures the torque required to rotate a spindle at constant speed while immersed in the sample fluid at constant temperature. Finally, the torque is converted to a dynamic viscosity and displayed on the screen. Fig. 53 shows a functional scheme of the Rotational Viscometer.

The measurement principle of capillary viscometer is simple. A piston pushes the fluid to test through a capillary of constant cross section under isothermal

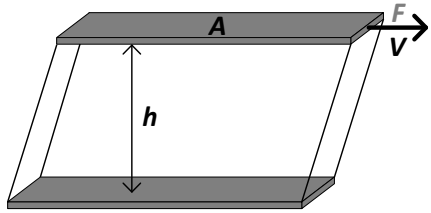

Fig. 51 Two plate Models, Shear rate

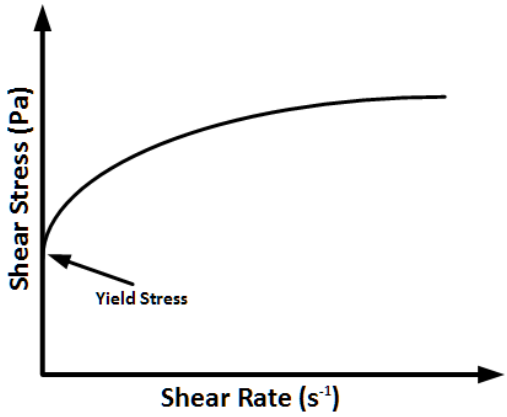

Fig. 52: Typical Rheogram with Yield stress point enlightened

condition. The volume flow rate, Q, and the pressure gradient, p, in the region of fully developed flow are measured for determining the shear viscosity. A drawing of a typical capillary viscometer is shown in Fig. 54.

Another instrument for the measurement of viscosity is the tube viscometer, which combines flow rate Q and pressure difference ΔP to measure the viscosity. A schematic of the tube viscometer concept for Newtonian fluids is depicted in Fig. 55.

The Shear Rate $\dot{\gamma}$ and Shear Stress τ are obtained by:

$$\dot{\gamma} = \frac{4Q}{\pi R^3} \qquad (50)$$

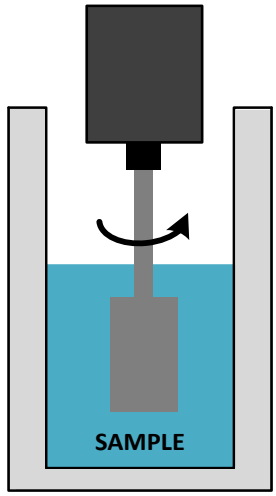

Fig. 53: Rotational Viscometer

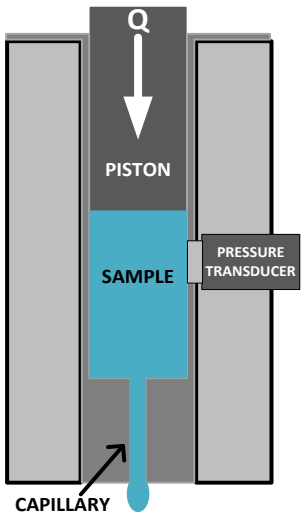

Fig. 54: Capillary Viscometer

$$\tau = \frac{\Delta \mathrm{P} \mathrm{R}}{2\mathrm{L}} \qquad (51)$$

Finally, the viscosity is:

$$\eta = \frac{\tau}{\dot{\gamma}} = \frac{\Delta \mathrm{P} \pi R^4}{8QL} \qquad (52)$$

Where Q is the flow rate, R the radius of the pipe, ΔP the differential pressure on the pipe and L the length of the pipe.

Rheological characterization using classical approaches is however time consuming and impractical for process control as several pipes with different diameters are used.

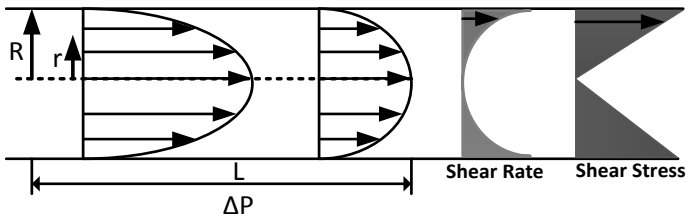

Fig. 55: Tube Viscometer.

4.2.2. Multi-gate Doppler Ultrasound Velocimetry

To assess rheological parameters of the fluids by classical methods, specimens are collected at different levels of the production chain and moved to laboratory, where they are characterized with viscometers. This process is performed only on discrete samples. In other cases, moving samples to the laboratory is not possible because the rheological parameters depend on the configuration present on the production plant and change rapidly in time. For all these cases, an electronic apparatus capable of continuous, inline, automatic rheological measurement is highly desirable [37]. An efficient, method for in-line fluids characterization of a wide range of non-Newtonian and opaque fluids exploits ultrasounds to detect the velocity profile of the flow moving in the pipe. The profile data, combined with pressure measurements, allows an accurate rheological characterization according to the Multi-Gate Pulsed Ultrasound Velocimetry (MDUV) + Pressure Drop (PD) method [38]–[46] .

The technique consists of transmitting a burst $St(t)$ every Pulse Repetition Interval (PRI) into the medium. When a moving particle encounters the burst, the produced echo is affected by a frequency shift, correlated to the particle axial velocity component, according to the Doppler effect:

$$f_{\mathrm{d}} = \frac{2 f_{\mathrm{t}} v_{\mathrm{z}}}{c} \qquad (53)$$

$$v_z = |v| \cos\theta \qquad (54)$$

where f_{d} is the Doppler shift frequency, θ is the angle between the ultrasound beam and the flow direction, v_{z} is the axial component of the velocity v, f_{t} is the transmitted ultrasound frequency and c is the sound velocity in the medium. The spatial velocity distribution along the axis of an emitted pulse beam can be obtained by measuring the Doppler shift at hundreds or thousands of depths aligned along the beam. For a single scatterer, which is moving with an axial velocity v_{z}, the analytical description of the echo signal $S_e(t)$ is:

$$S_e(t) = y(t) e^{j((\omega_{\mathrm{t}} - \omega_{\mathrm{D}})t + \varphi_0)} \qquad (55)$$

Where $\omega_{\mathrm{D}} = 2\pi f_{\mathrm{d}}$, $\omega_{\mathrm{t}} = 2\pi f_t$, φ_0 is the initial phase and $y(t)$ depends on the transmission signal $S_t(t)$, the attenuation of the medium and the system's impulse response. The Phase-Quadrature (IQ) demodulation is applied to the analytical echo signal for shifting the frequency and to obtain the complex base band signal $S_b(t)$:

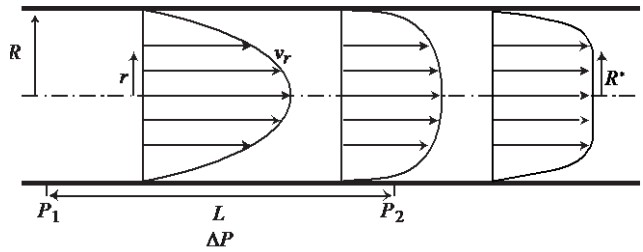

Fig. 56: Three different pipe flow velocity profiles. From left to right: (1) parabolic flow profile of a Newtonian fluid (viscosity independent of shear rate) (2) shear thinning fluid with flattened profile and (3) fluid with yield, resulting in a plug flow.

$$S_b(t) = S_e(t)e^{-j(\omega_t)} = y(t)e^{-j(\omega_D \cdot t + \varphi_0)} \qquad (56)$$

In each PRI, the in-phase (I) and quadrature (Q) components of $S_b(t)$ are stored along the columns of a matrix. When enough PRIs are stored, the data are read out by row, which represents the Doppler samples collected at same depth. The sum of the square of the spectrum, is performed on the weighted read out data, to obtain the power spectrum $f_b(f)$. A weighted mean is performed on every spectrum to obtain a single Doppler frequency from each depth:

$$f_{\mathrm{pm}} = -\int f_b(f) \cdot f \cdot df \Big/ \int f_b(f) \cdot df \qquad (57)$$

The velocity can be finally obtained by applying (53) to the measured f_{pm}.

For the fluids that flow in a pipe, the shape of the velocity profile, i.e. the velocity distribution across the pipe diameter, depends on the rheological properties of the fluid [47]. Newtonian fluids such as oil or water have a simple parabolic velocity profile, (Fig. 56 left) while non-Newtonian fluids (suspensions, etc.), with a shear rate dependent viscosity, develop different profile shapes. For example, shear thinning fluids present a flattened profile (Fig. 56, middle) and fluids with a yield stress produce a plug flow (Fig. 56, right).

For simple Newtonian fluids, the rheology is often determined from the volumetric flow rate and the pressure difference over a fixed distance of pipe. This is the method of the tube viscometer explained in the final part of 4.2.1. For non-Newtonian suspensions, which constitute 95% of all industrial fluids [37], the shear viscosity must be determined as a function of the shear rate. In tube viscometer, this means that the measurements must be performed in several different pipe diameters or at several different flow rates. In the enhanced tube viscometer concept, the flow profile shape is used to derive the shear rate dependent viscosity at the different shear rates present in the fluid. The shear rate $\dot{\gamma}$ along the radius *r* is the derivative of the flow velocity *v*.

$$\dot{\gamma}(r) = -\frac{\mathrm{d}v}{\mathrm{d}r} \quad (58)$$

Combining the information from the measured pressure drop and flow velocity profile it is possible to calculate the shear rate dependent viscosity η in real-time:

$$\eta(r) = \frac{\tau(r)}{\dot{\gamma}(r)} \quad (59)$$

4.3. MDUV System

The system includes all the electronics necessary for processing and conditioning the ultrasound signal. It is very compact (10 × 12 cm total dimension), low power (5 W max.) and made up of two boards: The Analog Front-End and the Digital Board [35], [48], [49]. The system is connected to a board of the sbRIO family (National Instruments, Austin, TX), which includes an Ethernet network connection. The software running on the industrial PC sets the working parameters and has access to the raw echo data, the demodulated data, the spectral matrices and the final normalized frequency profiles. The main features of the system are listed in TABLE III.

4.3.1. Hardware Architecture

The analog front-end is subdivided in two equivalent channels, shown in Fig. 57. The transmission section (Tx) of each channel amplifies the transmission burst

TABLE III: MAIN FEATURES OF THE ON-BOARD ELECTRONICS

Features	***Value***
TX/RX channels	*2, multiplexed*
Dimension	*10 × 12 cm*
Power consumption	*5 W max*
Analog Gain	*7 – 55 dB*
Tx voltage	*10 – 80 Vpp*
TX/RX frequency range	*1 – 7 MHz*
TX burst	*Arbritary waveform*
Internal buffer	*64 MB*
Sampling Freq.	*100 MHz*
Processing time	*42 µs/depth*
Input noise on 50 Ohm	*1.5 nV√Hz*
On board Proc.	*RF and IQ data, Spectral Matrix, Fequency Profile*

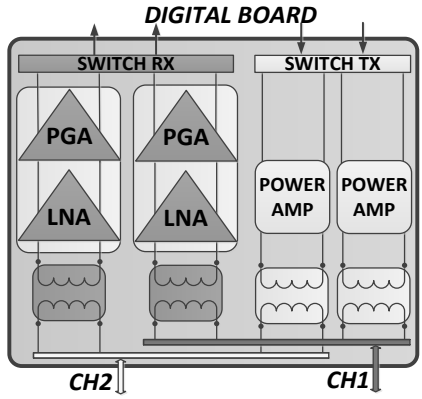

Fig. 57: Analog Board with ultrasound front-end. Switches are used in TX/RX to manage 2 different transducers

by a current feedback linear amplifier, the output can reach 27 Vpp, and a transformer raises the signal up to 80 Vpp and adapt the amplifier output to the transducers impedance. The Tx devices are turned on only during the transmission to minimize the noise and optimize the power consumption. The receiving section (Rx) amplifies the backscattered echoes and consists of an impedance matching transformer and a single chip, which integrates a Low Noise Amplifier (LNA) and the Programmable Gain Amplifier (PGA), which, together, produce a gain from 7 to 55 dB with bandwidth between 0.8 and 7 MHz. The selection of the Rx and Tx channels is managed by switches, controlled by the Field Programmable Gate Array (FPGA), located on the Digital board.

The Digital Board, shown in Fig. 58, is based on the EP3C25F256 FPGA from the Cyclone family of Altera (San Jose, CA), which manages all the digital devices present on the board.

During the transmission, the burst is generated with programmable amplitude, frequency, number of cycles and tapering, by a Digital Direct Synthesizer (DDS)

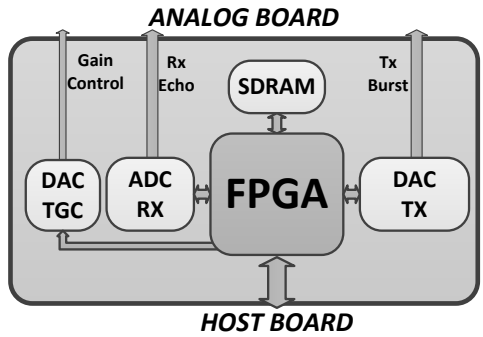

Fig. 58: Digital Board. A FPGA manages all devices.

Fig. 59: MDUV system: Analog front-end Board and Digital Board.

implemented on the FPGA. The burst is then converted by a 14-bit resolution, 100 MSPS Digital to Analog Converter (DAC) and sent to the analog front end. During the reception phase, the conditioned echoes are digital converted by an AD9265 (Analog Devices, Norwood, MA) at 100 MSPS with 16-bit resolution and finally, the data are processed in the FPGA. Fig. 59 shows the analog front-end board installed on top of the digital board that composes the MDUV system.

4.3.2. FPGA Firmware

The FPGA processing chain is reported in Fig. 60. Samples are coherently demodulated [50] by a multiplication to two, 16-bit resolution, quadrature-phase sinusoidal signals, which have the same frequency as the transmission burst. The resulting 32-bit, in-phase (I) and quadrature (Q) components are filtered by a Cascaded Integrator Comb (CIC) filter with a programmable cut off frequency and down-sampling factor. The filtered samples are stored in the 64 MB SDRAM

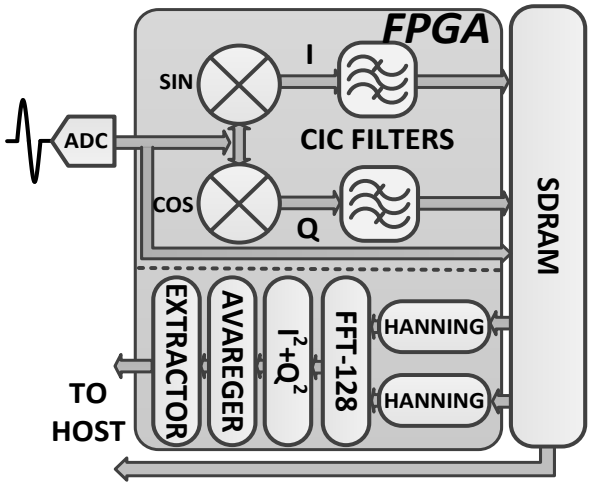

Fig. 60: Signal processing chain for real-time profile calculation implemented in the FPGA.

buffer at 32+32 bit per complex sample. The data storage strategy is shown in Fig. 61, where $D_{L,N}$ is the sample collected at pulse repetition interval (PRI) N and depth L. When enough data are stored, the multi-gate spectral analysis starts, moving from the SDRAM to the FPGA blocks of 128 complex samples acquired from the same depth.

The Hanning window is applied to each block and a block-floating point complex FFT processes the results. The sums of the square of the FFT output, converted to 32-bit floating-point format, allow to obtain the power spectrum. All the available depths are processed and the results are stored in the rows of a Doppler spectral matrix. A programmable number of matrices are averaged for improving the signal to noise ratio before the frequency profile is extracted. From each row of the denoised spectral matrix, the spectral frequency profile n_d is calculated with a discrete version of (57):

	Pulse Repetition Interval →					
Depth ↓	$D_{0,0}$	$D_{0,1}$	$D_{0,2}$	….	$D_{0,n-2}$	$D_{0,n-1}$
	$D_{1,0}$	$D_{1,1}$	$D_{1,2}$	….	$D_{1,n-2}$	$D_{1,n-1}$
	….	….	….	$D_{L,N}$	….	….
	$D_{l-2,0}$	$D_{l-2,1}$	$D_{L-2,2}$	….	$D_{l-2,n-2}$	$D_{l-2,n-1}$
	$D_{l-1,0}$	$D_{l-1,1}$	$D_{l-1,2}$	….	$D_{l-1,n-2}$	$D_{l-1,n-1}$

Fig. 61: The 64 MB SDRAM of the system holds a matrix where acquired data are stored in columns and read by rows.

$$n_{\mathrm{d}} = \frac{1}{N}\sum_{i=0}^{N-1} i \cdot \left|C_{d,i}\right|^2 \Big/ \sum_{i=0}^{N-1} \left|C_{d,i}\right|^2 \qquad (60)$$

Where $C_{d,i}$ is the matrix element corresponding to depth d and FFT bin *i*, and *N* is the FFT size. The frequency profile is obtained by dividing n_d to T_{PRI}, i.e. the temporal length of the PRI. The frequency profile is moved to the PC where the velocity profile is finally calculated by applying (53) and the rheological parameters are extracted and shown in real-time.

The implementation on the FPGA of the processing chain reported in Fig. 60, was carefully checked for the achievable accuracy. This has been obtained by generating synthetic data in Matlab® (The MathWorks Inc., Natick, MA) that mimic the ultrasound signal received in a typical pipe investigation. The data refer to a 6 mm diameter pipe, insonated at 5 MHz, where a parabolic flow runs at 0.5 m/s. Such data were processed both in the FPGA and in Matlab®. Fig. 62 compares

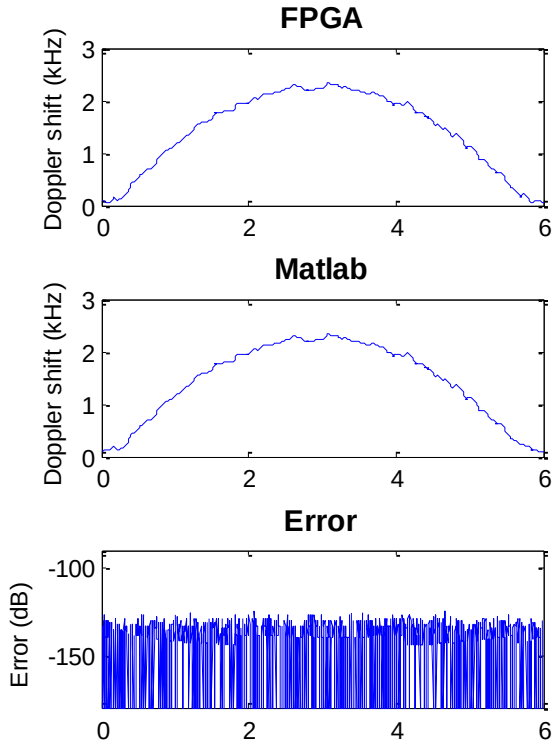

Fig. 62: Frequency profile calculated in the FPGA (top) and in Matlab® (middle) starting from the same RF data. The relative difference is reported on bottom in dB scale.

the velocity profile calculated by FPGA (top) to the reference obtained in in Matlab® in double precision math (middle).
The bottom of Fig. 62 reports the relative difference calculated as:

$$Err(n) = 20\log_{10}\left(|X_F(n) - X_R(n)|/X_R(n)\right) \quad (61)$$

where $X_F(n)$ and $X_R(n)$ are the profiles calculated in the FPGA and Matlab®, respectively. The error was always lower than -140 dB, which confirms the correct FPGA implementation of the processing chain.

.

4.4. Flow-Viz™ Characterization System

In this chapter the embedded in-line fluids characterization system, Flow-Viz™ [51], [52], specifically designed for the in-line velocity profile measurements and rheological assessment of opaque, non-Newtonian industrial fluids is described. The MDUV electronics is an essential part of the Flow-Viz™. Ultrasound transducers developed and optimized for SS316L stainless steel process pipes of different diameters and wall thicknesses [53], [54] are used. The Flow-Viz™ system consists of three main components:

- Operator's panel
- Sensor unit
- Software

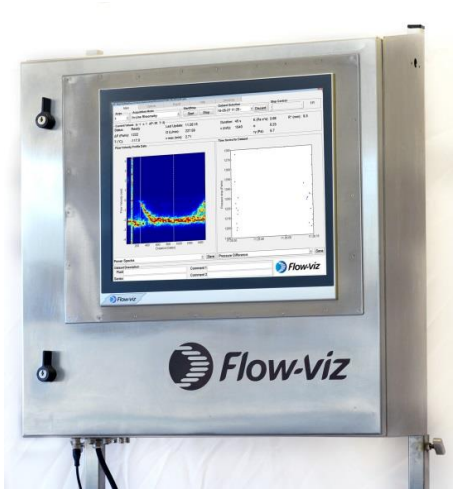

Fig. 63: The Flow-Viz™ operator's panel featuring the electronics, main Industrial PC unit and multi-touch monitor.

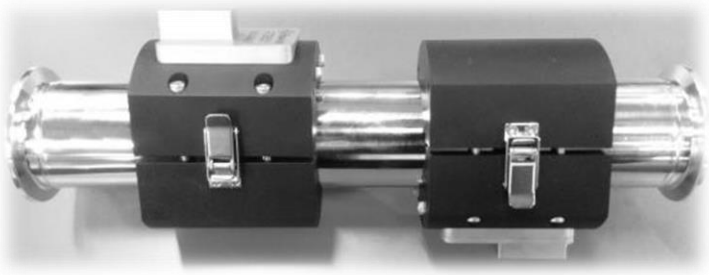

Fig. 64: The Flow-Viz™ noninvasive sensor.

4.4.1. Operator's Panel

The operator's panel, depicted in Fig. 63, houses the newly developed hardware platform composed of the MDUV electronics and data acquisition (DAQ) electronics, power supply, a 19"-multi-touch monitor, a sensor connector block and an industrial PC unit (Beckhoff Automation, Germany), that embeds a 2.5 GHz Intel® Core™ i7 quad-core CPU with CFast and SSD memory cards, 8GB RAM, 6 USB 3.0 ports and 2 independent Gbit Ethernet interfaces for remote control. The built-in 19"- monitor offers a user-friendly interface with multi-touch gesture navigation.

4.4.2. Sensor Unit

The sensor unit holds all of the sensors, is installed in the process network and makes up the measuring section [53], [54]. The measuring section is equipped with at least one pair of custom made, non-invasive ultrasound transducer (Fig. 64) assemblies (Flow-Viz™, Sweden), a differential pressure sensor with remote seals (ABB Automation Technology Products AB, Sollentuna, Sweden) and a non-invasive PT-100 sensor (Pentronic, Gunnebo, Sweden). The sensor unit

Fig. 65: The Flow-Viz™ Sensor unit.

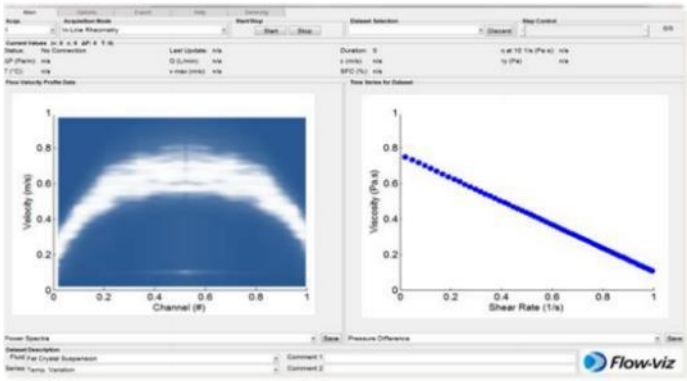

Fig. 66: The Flow-Viz™ GUI software interface,

typically comprises also a stainless-steel cabinet (Fig. 65) protecting the heat-jacketed stainless steel pipe with diameters ranging from 10 to 200 mm.

4.4.3. Software

The Flow-Viz™ system comes with a user-friendly GUI software interface optimized for the multitouch gesture monitor. The software is used for setting the parameters, controlling the data acquisition, signal-processing and for visualization and export of the data. The data is stored in an SQL database. A result display screen sample is shown in Fig. 66.

4.4.4. Electronics

A Motherboard (Schmid Elektronik AG) embeds the MDUV electronics and provides filtering and stabilization of the power, 8 analog and digital input and output channels; 4–20 mA, 0–10 V, /-5 V; 16 Bit, 4 PT100 circuits and serial ports. The Communications board is a National Instruments (NI) sbRIO-9606 module. The sbRIO board has a 400MHz processor, a Field-Programmable Gate Array (FPGA), 96 DIO lines and provides Ethernet, RS232, CAN and USB connectivity. The IOs on the base board are controlled from the FPGA on the sbRIO. The electronics enables simultaneous ultrasound velocity profile, pressure and temperature acquisition and signal processing from multiple sensors. It also provides real-time communication capabilities to an industrial PC.

4.5. Experiments and Results

In this chapter, experimental tests and results obtained by MDUV system are presented. They include, first, the measurements of the fluid composed of demineralized water and plastic particles. Then, the Rheological characterization

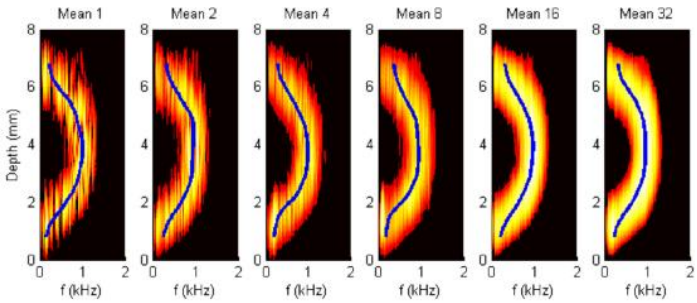

Fig. 67: Spectral matrices calculated by the MDUV board when investigating a fluid flowing in a 6 mm diameter pipe. The fluid was composed by 10 μm diameter plastic particles suspended in demineralized water. The MDUV was programmed to average 1 to 32 spectral matrices for frame (from left to right). The frequency profile calculated by the MDUV board is superimposed in blue in each frame.

of the industrial fluids obtained by Flow-Viz™ system, where the MDUV system has been successfully installed, are reported.

4.5.1. Velocity Profile Measurements

Fig. 67 shows, for example, the Doppler spectral profile matrices obtained by investigating a flow in a 6 mm pipe with 5 MHz bursts fired at PRI = 0.5 ms by a transducer positioned at 60° with respect to the axis of the pipe. A peristaltic pump was used to recirculate a fluid at 500 mℓ/min. The fluid was constituted by degassed water with dissolved 10μm diameter plastic particles, capable of generating a suitable echo to the ultrasound burst transmitted by the MDUV system. The frequency profile extracted by the Doppler spectral matrix is displayed from left to right, with no-averaging and averaging of 2, 4, 8, 16, 32 matrices, respectively. The frequency profiles, calculated by the MDUV system, are superimposed to the corresponding spectral matrices. As expected, the profile is roughly parabolic and the maximum flow velocity is around the middle of the vessel. [55], [56].

4.5.2. Rheological Fluids Characterization

In the Flow-Viz™ system the velocity data measured from the wall to the center of the pipe is differentiated and the resulting shear rate vector is used in combination with the pressure drop to determine the fluid rheology. A non-Newtonian industrial fluid with a particle concentration of 26% (w/w) flowing in a SS316L stainless steel pipe with an inner diameter of 48.6 mm was measured with the Flow-Viz™ system to verify that the penetration depth and data quality is acceptable for rheological characterization of the fluid. The flow rate was set at

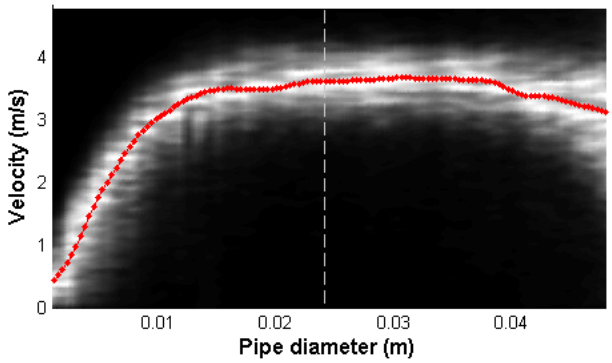

Fig. 68: Spectral matrix and velocity profile (overlapped in red) obtained from an industrial fluid, measured at a volumetric flow rate of 6L/s in a pipe with an inner diameter of 48.6 mm.

6 L/s. The system calculated in-line 32 profiles/s with a spatial resolution of a few µm. Fig. 68 shows a calculated spectral matrix with the velocity profile overlapped. The penetration depth reached the full pipe diameter even in this highly attenuating (about 5 dB/cm) industrial fluid. The corresponding complete rheogram is shown in Fig. 69, where shear rate and shear stress are directly obtained from the measured data.

The yield stress for many industrial applications is an important quality control parameter that is difficult to determine using conventional techniques. The yield stress, obtained directly from the measured plug radius, was equal to 8 Pa, which is in excellent agreement with 8,1Pa refernce determined using a stress controlled viscometer.

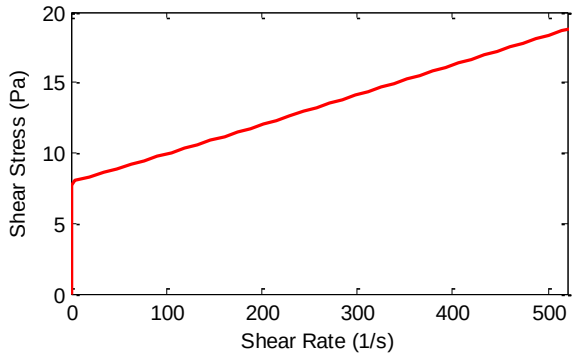

Fig. 69: Rheogram measured in-line by the system in a non-Newtonian fluid with 26% particle concentration. The yield stress was obtained directly from the measured plug radius and equal to 8 Pa.

In general, the rheograms provided by the Flow-Viz™ system is within a 5% when compared with rotational viscometer data [57].

4.6. Discussion and conclusion

This work presents the Multi-Gate Doppler Ultasound Velocimetry (MDUV) embedded in the Flow-Viz™ system, which is an integrated digital in-line fluids characterization system for industrial and research applications that is now commercially available.

The MDUV electronics features an Analog Front-End and a Digital Board that offers on-board processing and velocity estimation capabilities, and a baseboard with 8 analog and 10 digital I/O DAQ channels for simultaneous acquisition and processing of e.g. pressure and temperature signals. The possibility to acquire data at 100 MHz allows a very high spatial resolution. The system calculates the frequency profile in 42 µs per depth (e.g. a 512-depth profile is generated at 45 Hz rate), with no need of further processing on host side. The host can access raw data, I-Q demodulated data, spectral matrices, and the frequency profile. The combination of fixed-point, block floating point, floating-point math representation in the receive processing chain allows a high dynamic with an error lower than -100 dB for spectral matrices and few mHz in the calculation of the frequency profile. A strong effort was paid to improve the system sensitivity by reducing the input noise: the LNA section of the board is completely shielded, an 8-layer PCB is used to better isolate the potential sources of noise, and every non-necessary device is switched off during the RX phase. These features allowed limiting the equivalent input noise to 1.5 nV/√Hz. Moreover, the on-board transmitter, based on AWG, can generate the coded excitations used in pulse-compression techniques [58], suitable to further improve the signal-to-noise ratio. The system is designed according to a full-digital approach. The analog conditioning is minimal and the signal processing is performed numerically in the FPGA. This method grants the maximum programmability and flexibility. The system in combination with the non-invasive sensors thus provide improved penetration depth and allows better possibilities to optimize the velocity resolution compared to other commercially available instruments. The measured profile is integrated and the determined flow rate is in general less than 5% from the flow rate determined using Coriolis flow meters.

The main limitation of the technique is that it requires scattering particles to be present in the fluid and it can thus not be applied e.g. to distilled water. The strong attenuation of ultrasound in highly concentrated suspensions could be another limitation and the choice of sensor design thus depends on the application.

Moreover, the system provides continuous data that allows the operator to make rapid adjustments of the processing parameters in the plant. However, today there is currently no support for handling the continuous feed of such quality control parameters in most production installations. The system is a useful characterization tool for field use, pilot plant installations and academic research, and has been successfully tested in a wide range of industrial applications, e.g. oil, petroleum, food, minerals, chocolate, explosive emulsions and pharmaceutical industry.

4.7. Contributions on Fluids Characterization

The work exposed in this chapter is published in the follows scientific papers:

1. Wiklund, J., Kotzé, R., Birkhofer, B., Ricci, S., **Meacci, V.**, Haldenwang, R., Stading, M.: Flow-VizTM-A fully integrated and commercial in-line fluid characterization system for industrial applications. 2014 9th International Symposium on Ultrasonic Doppler Methods for Fluid Mechanics and Fluid Engineering (ISUD) Proceedings. pp. 165-168 (2014).

2. Ricci, S., **Meacci, V.**, Birkhofer, B., Wiklund, J.: Embedded System for In-Line Characterization of Industrial Fluids. Applications in Electronics Pervading Industry, Environment and Society. (In press).

3. Ricci, S., **Meacci, V.**, Birkhofer, B., Wiklund, J.: Embedded system for in-line ultrasound velocity profile detection. 2015 IEEE International Ultrasonics Symposium (IUS) Proceedings, pp. 1-4 (2015).

4. Wiklund, J., Ricci, S., **Meacci, V.**, Kotze, R., Birkhofer, B. : Flow-Viz Pulsed Ultrasonic Doppler System with Auto Tuning of Analog-, Digital Gain and Threshold. 2016 10th International Symposium on Ultrasonic Doppler Methods for Fluid Mechanics and Fluid Engineering (ISUD) Proceedings, pp. 241-248 (2016).

5. Ricci, S., **Meacci, V.**, Birkhofer, B., Wiklund, J.: FPGA-based System for In-Line Measurement of Velocity Profiles of Fluids in Industrial Pipe Flow. IEEE Transactions on Industrial Electronics. 99, 1-1 (2016).

6. **Meacci, V.**, Ricci, S., Wiklund, J., Birkhofer, B., Kotze, R.: Flow-Viz - An integrated digital in-line fluid characterization system for industrial

applications. 2016 IEEE Sensors Applications Symposium (SAS) Proceedings, pp. 1-6 (2016).

7. Wiklund, J., Birkhofer, B., Ricci, S., **Meacci, V**., Stading, M.,: An integrated in-line fluid characterization system for industrial applications. Journal of Japan Society of Fluid Mechanics 34, 241-248(2015).

The first one, is the conference proceeding where the Flow-Viz™, that is the system used for characterizing opaque fluid in industrial environment is explained in details and measurements on industrial fluids are reported

The second, third and fourth are conference proceedings and a fifth is a journal paper where the designed ultrasound system use to evaluate the velocity profile of the fluid in a pipe is analyzed in details. All the features of the system designed during the years, are reported. Measurements obtained in laboratory and on field are discussed.

The sixth is a conference proceeding where the theory needed to evaluate velocity profile by ultrasound systems is explained in details and measurements obtained by the designed system are discussed.

The last one is a journal paper where the rheology theory needed to assess the property of the opaque industrial fluids and suspensions are explained in detail and results achieved by Flow-Viz™ are disclosed.

All contributions are reported in section 1.2.

Chapter 5. High Frame Rate Medical Imaging

In this chapter an Ultrasound System developed for researching purpose and a Novel Ultrasound Method for high frame rate imaging implemented in the system, are presented. The system and method allow investigating rapid phenomena in medical applications.

5.1. Ultrasound Medical Imaging

Ultrasound imaging uses acoustic waves to investigate human body, it's a noninvasive, safe and painless medical technique that uses non-ionizing radiations to help diagnose and treat diseases. The images show the internal structures of the human body as discussed in section 2.4.1.

5.1.1. Ultrasound Systems for Research

Experimental ultrasound research frequently involves original transmission strategies, non-conventional beamforming techniques, flexible data processing and huge data storage capabilities. Such features are not available in commercial clinical equipment, while full control of the transmit/receive operations and the access to raw echo data are possible in few open research platforms[59]. These features characterize the synthetic aperture real-time ultrasound system (SARUS), a unique research platform located at the University of Denmark, which is connected to a 144-core Linux cluster to manage up to 1024 channels and 128 GB of acquired data [60]. Commercial research scanners, even though not as powerful and flexible as the SARUS, are also available for laboratory and clinical use.
For example, BK Ultrasound (Richmond, BC, Canada) provides its top level diagnostic system, SonixTouch Research, with an ultrasound research interface that enables research-specific capabilities, such as modification of low-level parameters and beam sequencing. The system needs to be coupled to the SonixDAQ parallel channel data acquisition tool for acquiring raw ultrasound data [61]. Another example is the Aixplorer system (Supersonic Imagine, Aix en Provence, France), which stands out for its high-frame rate (HFR) capability. Its research version allows the acquisition of raw radio frequency (RF) data either before or after beamforming and the acquisition of HFR images for offline processing [62]. One of the most powerful commercial research scanners is the Vantage (Verasonics, Redmond, WA) that controls up to 256 independent channels. It offers programmable transmission based on three-level transmitters and allows access to the pre-beamforming samples. The Vantage system also provides the MATLAB interface to modify the signal and image processing parameters and to incorporate custom algorithms [63]. Another interesting example of open scanner using Graphics Processing Units (GPU) for real-time data processing is described in [64].

The ULA-OP, which was entirely developed at the University of Florence, is a research system characterized by an accurate balance among computational power, cost, dimensions, and flexibility [65]. By using only five Field Programmable Gate Arrays (FPGAs) and one Digital Signal Processor (DSP), it

is possible to integrate all of the needed electronics in two programmable boards, coupled to a host PC through USB 2.0 link. A powerful, compact, and relatively cheap architecture, capable of finely controlling 64 elements selected out of a 192-element array probe, was thus obtained. The fields of application of the ULA-OP span from vector Doppler investigations [66]–[70] to motion estimation [71]–[74], from nonlinear contrast imaging [75]–[77] to tissue characterization [78], [79]. The system was also employed to develop innovative beamforming schemes to improve the image quality [80], [81] to compensate for the refraction induced by skull bone [82]–[84] as well as to validate novel ultrasound image formation models [72], [85]. Although successfully used in many different applications, ULA-OP is not sufficiently powerful to satisfy all requirements of emerging methods, such as real-time HFR [86]–[88] or vector Doppler imaging [68]. Therefore, a novel portable platform characterized by a highest number of channels and computational power called ULA-OP 256 it was designed and developed.

5.1.2. Standard Imaging Techniques

An ultrasound probe is typically composed by several tens of piezoelectric transducers, located side-by-side to form an array antenna.

The echograph transmits an ultrasound pulse through the probe. The backs scattered echoes produced by the impedance discontinuities of the investigated tissue are received back by the same transducers, then amplified, Analog-to-Digital (AD) converted and processed in the Beamformer (BF) [2], [89]. The BF applies suitable delays and apodization coefficients to the signals acquired from each transducer of the probe, and then adds them to synthetize a receiving radiation field with the desired shape. According to the standard approach, for example, a B-Mode image is created by means of a focused ultrasound beam that sequentially scans hundreds of adjacent lines. The image frame rate (IFR) is limited of 30 to 70 Hz by the relatively low velocity of the sound travelling through the region of interest.

Unfortunately, this limit may hamper the investigation of morphological structures that rapidly move like, for example, the heart valves [90]. This bottleneck is particularly critical for scanning of 3D volumes [91], in which the number of lines can grow up to thousands.

5.1.3. High Frame Rate Imaging Techniques

To produce high frame rate images, the technique called Parallel beamforming [92] excites a relatively large region with a single transmission and simultaneously beamforms several M-lines from the acquired echo samples. This method allows an M-fold gain in IFR and, in its full implementation produces an IFRs of several kHz [93]. Unfortunately, it's quite complex and needs powerful, high-speed electronics. Moreover, in a real-time implementation, based on FPGAs, every Pulse Repetition Interval (PRI) the channel-data are acquired at 40-80 Msps and simultaneously beamformed at the same rate by M-parallel beamformers (BFs). However, since a single BF typically requires most of the resources of one of more large FPGAs, only bulky and costly systems can support this method.

An alternative approach consists in saving the data acquired from each channel in a large memory buffer. When the acquisition is stopped, the data can be downloaded and post-processed. In this way the acquisition produces a huge amount of data in few time, therefore, tens of Gbyte of high-speed memory are needed [94].

The proposed beamformer called Multi-Line Parallel Beamformer (MLPBF) is based on an architecture that processes in real-time multiple lines per PRI, thus enhancing the IFR by a corresponding factor. The proposed architecture exploits a combination of parallel and serial processing strategies, and is implemented in the modern FPGAs of the research scanner ULAOP256. In each PRI, data are acquired at sampling frequency Fs from up to 256 probe-elements, and stored in

Fig. 70: ULA-OP 256.

FPGA memories. The MLPBF reads the data, applies delays and coefficients, and produces a group of lines. This process, running at maximum speed, is repeated several times to beamform all lines, until the PRI ends.

5.2. ULA-OP 256

The Ultrasound Advanced Open Platform 256 (ULA-OP 256), which was entirely developed in our laboratory for research purposes, provides tools and power processing needed to implements novel investigation methods, both, in real time and post processing.

5.2.1. System Description

ULA-OP 256, shown in Fig. 70, has been designed to directly and independently control up to 256 TX-RX channels connected to linear or matrix probes, either Capacitive Micromachined Ultrasound Transducers (C-MUT) or piezoelectric. Real-time user-definable operation modes including innovative beamforming algorithms and strategies are supported. Access to raw data at any point of the RX chain, including data acquired by each probe element, is possible. High computational power and storage capability are achieved through extensive and optimized use of high-end devices. At the same time, efforts have been made to integrate the electronics in a limited number of boards, to facilitate system transportability.

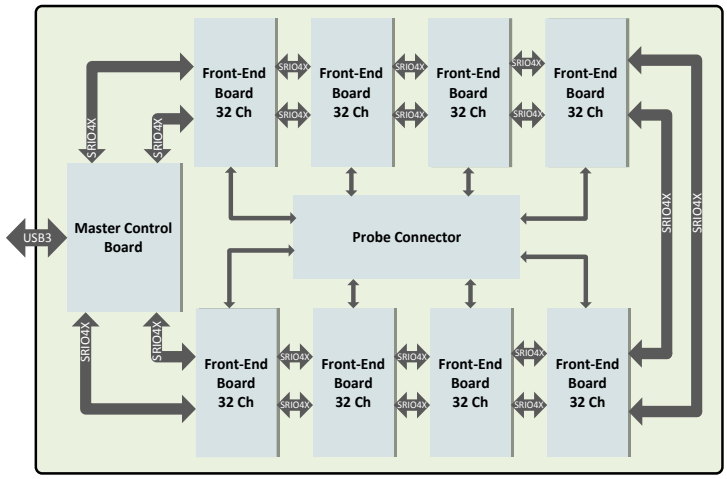

Fig. 71: General architecture of ULA-OP 256.

5.2.2. System Architecture

The architecture of ULA-OP 256 is based on the use of multiple front-end (FE) modules, each capable of controlling 32 probe elements. 256 ultrasound channels are thus managed by 8 FE boards, but a lower number of boards can be used in association to specific probes. One additional board, the Master Control (MC) board, manages the interaction between a host PC and the system by means of an USB 3.0 connection. The MC board hosts a multicore DSP from the TMS320C6678 family (Texas Instruments, Austin, TX, USA) featuring eight cores running at 1.2 GHz and up to 8 GB of DDR3 memory. One FPGA from the Cyclone V family (Altera, San Jose, CA, USA) manages the communication between USB and the system. All of the FE boards are interconnected by a SerialRapidIO (SRIO) link running at 5 Gbit/s on 4 lanes. Each board has 4 SRIO interfaces interconnected through a ring running on the system backplane. The total I/O bandwidth available for each board in the ring is thus 80 Gbit/s full duplex. Fig. 71 illustrates the general architecture of the system.

The FE module integrates all of the electronics needed to manage the TX, RX and real-time elaboration for 32 channels (Fig. 72). An on-board FPGA from ARRIA V GX Family (Altera, San Jose, CA, USA) is in charge of generating 32 TX analog signals with bandwidth up to 20 MHz. This generation is based on a sigma-delta approach that produces bit streams at 500 Mb/s rate. The ultrasound echo-signals received by the corresponding 32 elements are amplified and digitized at 80 MSPS with 12-bit resolution by four 8-channel ultrasound front-end ICs (AFE5807, Texas Instruments). A single FPGA (Beamforming FPGA) performs the delay and sum operations requested to beamform 32 channels. The board hosts two DSPs each equipped with up to 8 GB of DDR3 memory. The

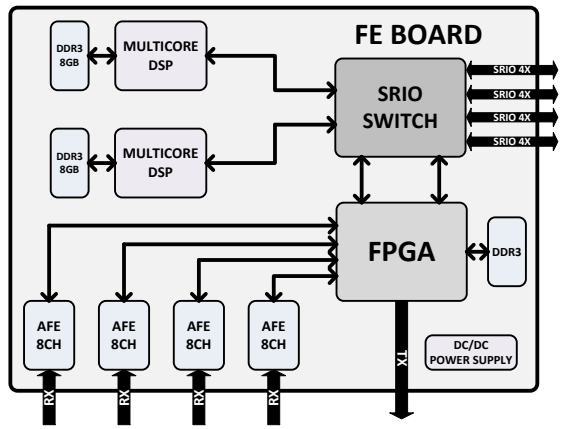

Fig. 72: Block Diagram of Front-End Board.

Fig. 73: Front-End Board.

DSPs are in charge of real-time processing in operations such as coherent demodulation and filtering, and a large class of custom elaboration modules can be added.

Real-time beamforming is performed in two steps according to the selected strategy. A first step is carried out by the Beamforming FPGA of each FE board (Fig. 73), and concerns a group of echo-signals from 32 elements that are suitably weighted, delayed and summed. Full 256 channels beamforming is achieved by appropriately summing the contributions from multiple FE boards. Every PRI, the FPGA sends the partially beamformed samples directly into the DDR memories of the DSP by means of the Serial Rapid IO (SRIO) link, as depicted in Fig. 74. Through the intensive use of DMA channels, the DSP schedules the processing of the N-lines in its 8 cores. Here, the unified computational capacity is nearly 700MSPS. If required by the application (e.g. compounding), the radiofrequency samples of M consecutive PRIs are summed together, then, the result is coherently demodulated at a programmable frequency, usually, but not necessarily, matching the central transmission frequency, low-pass filtered by a cascade of four averaging filters and down-sampled to produce 512 quadrature base-band samples per line. Through the SRIO link, these are sent to the Master Control (MC) board, where the samples coming from up to 8 boards are accumulated to perform the last stage of beamforming inside the on-board DSP. This DSP stores the final

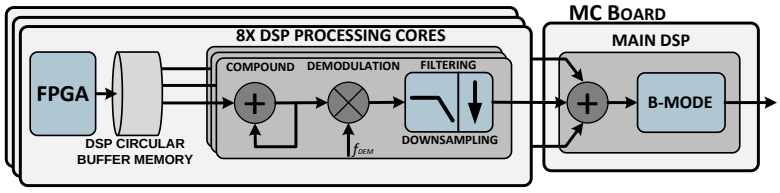

Fig. 74: Data flow and processing, from the FE FPGA beamformers to the host PC for display.

samples in a large (up to 8GB) DDR3 memory. Data can be downloaded to the PC, once the acquisition is stopped. During acquisition, the DSP processes data in real-time to produce B-Mode frames of 64x512 points. The 256-level gray-scale frames are buffered and sent through a USB3.0 connection to the PC for real-time display. Moreover, Radiofrequency (RF) raw data, post beamformed RF data or quadrature demodulated (baseband) signals can be collected to store them in a huge amount of memory, 80GB of DDR3 (expandable up to 144 GB) when 8 FE modules are installed.

The ULA-OP 256 is managed by a modular and configurable software running on the host PC. This software initializes the hardware upon startup, provides a user-friendly interface and displays the results of ultrasound data elaboration on the screen. The system can be programmed by means of text configuration files. These files, easily and quickly modifiable by the user, provide the main startup settings for all of the resources in the system. Once ULA-OP 256 is configured, the acquisition begins and the real-time processing results are displayed on the screen. By operating on the control panels of the software, the users can change several processing parameters on the fly, and immediately observe the related effects. Moreover, the user can stop the acquisition at any time and store in binary files any data so far collected. Every time the software needs to configure or change a parameter in the system, a command is transmitted by the PC through the USB link, and received by a DSP on ULA-OP 256. The DSP interprets the command and eventually modifies its parameters or forwards the adjustment to other programmable devices such as the FPGAs.

5.3. Beamforming

Beamforming is a signal-processing technique used in various applications such as wireless communications, radar, and sonar that uses an array of transducers or elements for transmitting and receiving electro-magnetic or acoustic waves.

In medical ultrasound, beamforming is used to electronically focus the transmitted and received signals as explained in section 2.3.

5.3.1. Classical Beamformer

Conventional ultrasound B-mode image is composed by multiple lines obtained by scanning the tissue in which acoustic waves propagate (5.1.2). For each line, the system excites the transducer elements with, typically, a short sinusoidal burst with frequency in the range 1-10MHz. By applying suitable delays, the Transmission Beamformer produces a thin beam focalized in the desired point

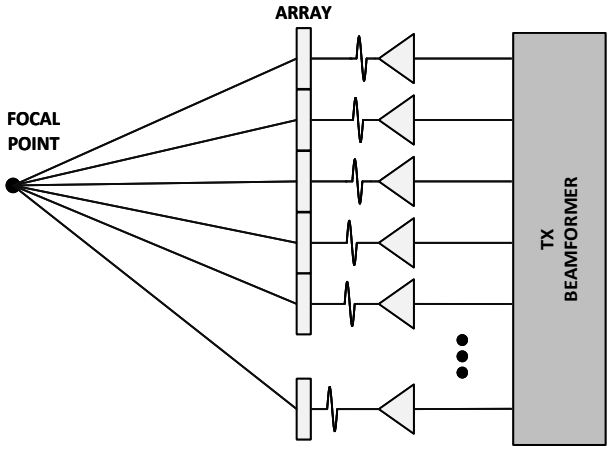

Fig. 75: Conventional beamformer, transmission section.

(Fig. 75). During reception (Fig. 76), the backscattered signal is amplified and digitized at a sample rate F_S= 40-80 Msps.

The reception Beamformer, then applies different apodization coefficients (APOD in Fig. 76) to all the acquired signals form the probe elements. Finally, the signal acquired from each transducers is delayed by a suitable quantity that dynamically changes with the depth of the origin (Dynamics Focusing) [1]. The result is that the signal is focalized in every point of a line, rather than in a single point. Apodization and delay coefficients are pre-calculated and stored in memories, while the delays are applied with digital delay chains realized through memories (e.g. FIFO in Fig. 76).

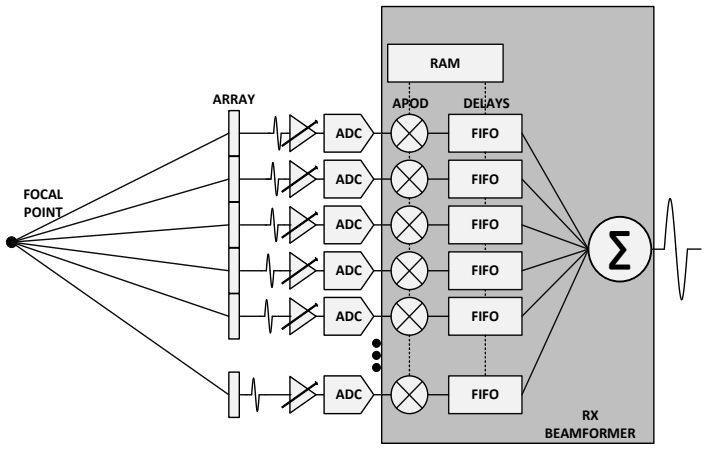

Fig. 76: Conventional beamformer, reception section.

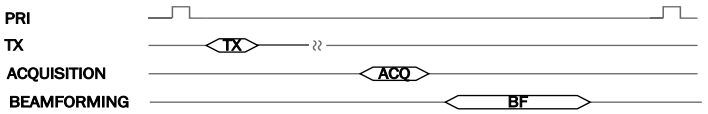

Fig. 77: Conventional Beamformer temporal sequence of operations

All these operations are quite calculation-intensive and are typically devoted to fast FPGAs, which generate each point of the image at the same rate used for data sampling, i.e. F_S.

In the classical approach an ultrasound burst is transmitted every PRI and the corresponding line is beamformed before next transmission occurs (Fig. 77). The minimum duration of the PRI is equal to *2d/c*, i.e. the time necessary to the acoustic wave to reach the maximum investigated depth, *d*, and travel back to the transducer (c ≈ 1500 m/s). Since an *N-line* image requires *N* PRIs, the maximum Image Frame Rate (IFR) achievable through the standard BF is:

$$\mathrm{IFR}_s = \frac{1}{N}\frac{1}{PRI} = \frac{c}{2d}\frac{1}{N} \qquad (62)$$

Due to the limited velocity of the sound in tissues, the duration of each PRI is typically in the order of 100µs. To create an image composed by, e.g., 200 lines, 200 PRIs are needed, thus limiting the image frame rate (*IFR*) some tens of Hz.

5.3.2. Parallel Beamformer

To increase the IFR a different transmission/reception strategy can be employed. The direct implementation of a parallel beamformer [95] (Fig. 78) simultaneously beamforming multiple lines of the B-mode image as explained in section 5.1.3.

According to this strategy, a B-mode frame can be theoretically obtained in a single PRI, and the IFR can reach 1/ *PRI* (Fig. 79). The electronics that performs the aforementioned operations is simply replicated M times, one for each line that should be simultaneously obtained. Beamforming many tens of lines during a single PRI requires awkward calculation efforts. Although this approach grants the maximum IFR, it is inefficient in several parts. First, the calculations are performed at a rate much lower than the frequency allowed by modern devices, which can be as high as some hundreds of MHz. Second, since the acquisition window is typically shorter than the PRI temporal length (see "ACQ" in Fig. 79), the BFs work with low duty-cycle, being unused for most of the time.

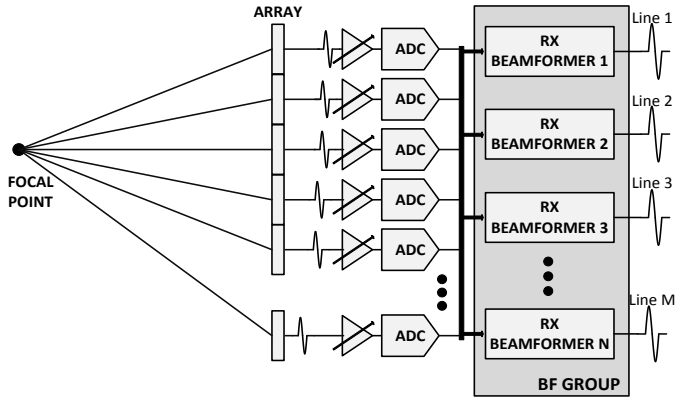

Fig. 78: Architecture of parallel Beamforming.

5.3.3. Multi-Line Parallel Beamformer

In MLPBF (5.1.3), a large region is excited by one unfocused beam transmitted every PRI, (for example a plane wave) then all the *N*-lines of the image are beamformed before the next transmission occurs. A large Dual-Port Memory (DPM) is placed between the AD converters and the FPGA section where mathematical calculations are performed (Fig. 80). The DPM is used for storing the data acquired at the sample frequency Fs. The data acquisition takes the time:

$$T_{acq} = \frac{2d}{c} \qquad (63)$$

When the first burst of 32 acquired data is stored in the DPM, the BFs starts to process the first group of lines working at the maximum frequency allowed by the device, i.e. F_M. Once the first group of lines is generated, the data in the DPM are read again and processed by BFs, which uses different coefficients to obtain a new group of lines; and so on, until all the lines of the image are processed. A group

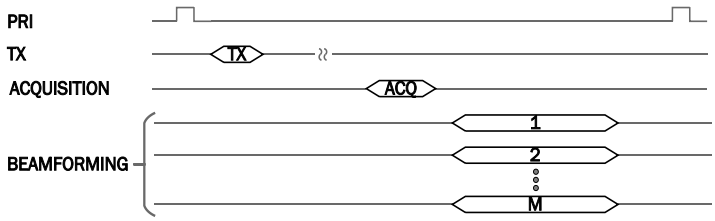

Fig. 79: Parallel Beamformer temporal sequence of operations.

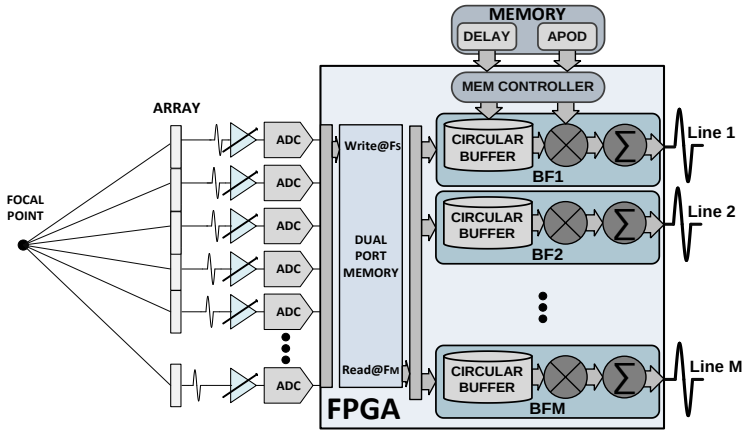

Fig. 80: Multi-Line Parallel Beamformer architecture.

of lines, where N_p is the number of the of samples per line, are processed in a time T_b:

$$T_b = \frac{N_p}{F_M} \qquad (64)$$

The time required for calculating the N-1 lines of the image by N_B beamformers is:

$$T_{nb} = \frac{N-1}{N_B} \cdot T_b = \frac{(N-1)}{N_B} \cdot \frac{N_p}{F_M} \qquad (65)$$

N-1 factor, since the first line is processed during the acquisition in a time T_{acq}.The total time between successive transmissions is T_{acq}+T_{nb}, thus the maximum frame rate achievable by MLPBF is:

$$\mathrm{IFR}_m = \frac{1}{T_{acq} + T_{nb}} = \frac{c \cdot F_M \cdot N_B}{c \cdot (N-1) \cdot N_p + 2d \cdot F_M \cdot N_B} \qquad (66)$$

The gain with respect to the standard approach, is:

$$\mathrm{G} = \frac{\mathrm{IFR}_m}{\mathrm{IFR}_s} = \frac{2d \cdot F_M \cdot N \cdot N_B}{2d \cdot F_M \cdot N_B + (N-1) \cdot N_p \cdot c} \qquad (67)$$

For example, in case of *d*=10cm, *Np*=2048, *N*=96, N_B=4 F_s=80MHz and F_M=200MHz, the IFR are:

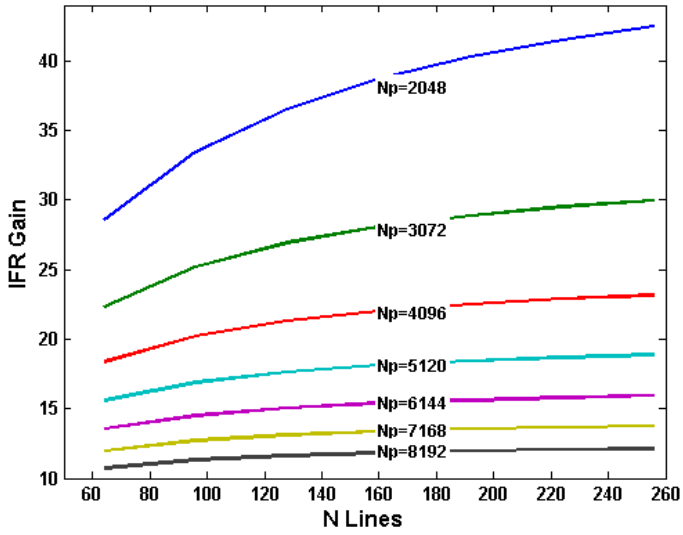

Fig. 81: IFR Gain of Multi-Line Parallel beamformer in relation to the Number of lines, N and the number of samples along depth, N_p, when F_S=80MHz, F_M=200MHz, N_B=4 and d=10cm.

$$\mathrm{IFR}_s = \frac{c}{2d}\frac{1}{N} \approx 78\mathrm{Hz} \qquad (68)$$

$$\mathrm{IFR}_m = \frac{c \cdot F_M \cdot N_B}{c \cdot (N-1) \cdot N_p + 2d \cdot F_M \cdot N_B} \approx 2.7k\mathrm{Hz} \qquad (69)$$

In this case, the IFR_m produced by MLPBF is about 33 times the IFR_s produced by the conventional BF.

Fig. 81 shows how the gain, G, changes in relation to the number of lines per image, N, and the investigation depth in terms of the number of points, Np. G, is evaluated with F_S=80MHz, F_M=200MHz, N_B=4 and d=10cm. The figure shows that the number of lines has a relatively low impact on the gain. On the other hand, G sensibly grows when the number of acquisition points decreases. This is related to the reduction of the time T_b (64) necessary to beamform each line.

The processed data are stored in the BF Data Buffer before being transferred to high level processing unit (e.g. Digital Signal Processor).

5.4. Implementation of Multi-Line Parallel Beamforming

The Multi-line parallel beamformer was implemented in ULA-OP 256. It is composed by four identical sections of a multi-line sequential beamformer (BF). The BFs operate in two clock domains. The acquisition domain works at the AFE sampling frequency, F_S (78.125 MHz), possibly reduced by a down sampling factor of 1, 2, 3 or 4, which is used when the highest sampling frequency is not needed. The processing domain is set at the FPGA maximum clock frequency, F_M (234.375 MHz). A dual-port memory (DPM) is used for crossing the two clock domains: all of the echo data acquired in the current PRI are written into one port at the actual sampling frequency, F_S, while they are read from the other port at rate F_M. The DPM stores 8192 words of 384-bit each (corresponding to 32 channels at 12 bit per sample) of the echo signal for each cycle of the acquisition clock. During each PRI, the digital samples are stored into the DPM and immediately read back by the BFs to process the first sub-group of lines during the receiving phase.

The results of the beamforming are sent to the subsequent electronics for further processing. At the end of the echo data acquisition, the data in the DPM are read-out again and processed by the BFs, now at the frequency F_M. Different beamforming coefficients are used to produce the second group of lines. The process is repeated until all of the image lines are processed. A dedicated controller manages the access to the DDR memory bank, which stores the delay and apodization coefficients.

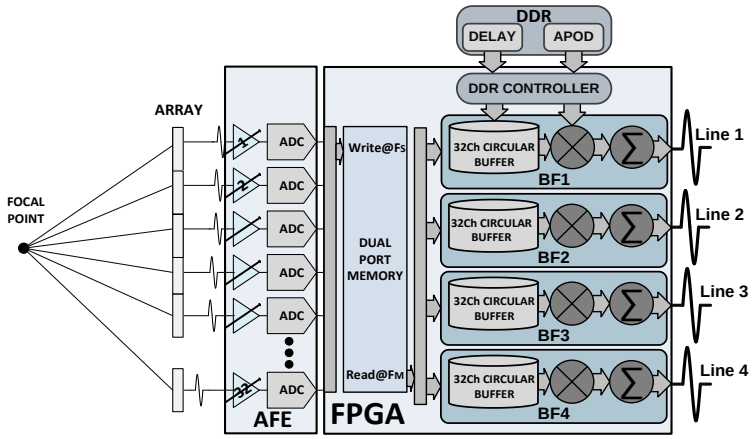

Fig. 82: implemented architecture of Multi-Line Parallel Beamformer.

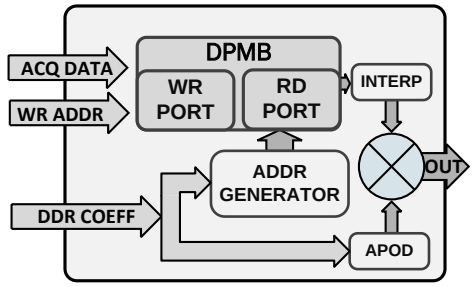

Fig. 83: Multi-Line Parallel Beamformer single block

The controller, which works at F_M, initializes the memory devices, produces the refresh commands at appropriate intervals and translates the read and write requests from the local interface to DDR commands.

The architecture of a single BF (Fig. 82) consists of 32 identical single channel blocks, one for each acquisition channel.

Every block (shown in Fig. 83) embeds a circular buffer synthesized with a Dual Port Memory Block (DPMB), an address generator (AG), a sample interpolator (INTERP) and a multiplier for the apodization coefficients (APOD). The DDR controller sends the delay coefficients to the AG, which generates the read address for the DPMB that corresponds to the desired delay. The apodization controller

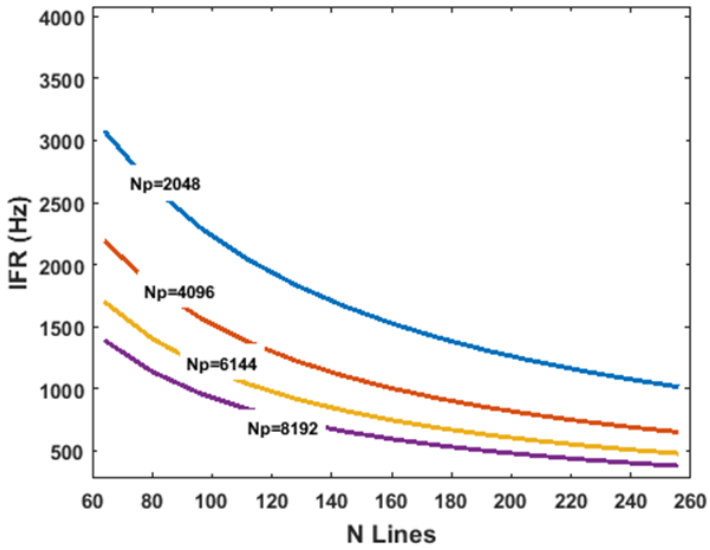

Fig. 84: Image frame Rate (IFR) with 4 beamformers in function of the number of lines, N and the number of samples per line, Np, when F_S =78.125MHz, F_M=234.375Hz and the maximum analyzed depth is 8 cm.

generates the apodization values from the DDR bit-stream. The data read from DPMB are interpolated with resolution of 1/16 of the sampling period to produce more accurate beamforming delay values. They are then multiplied by the apodization values and finally summed with the output generated by the other blocks. When the circular buffer has been completely read, every point of the line has been calculated and the BF restarts the process to produce the next line. During this activity, the beamformed data are continuously transferred to subsequent electronics for high-level processing.

Fig. 84 reports the Image Frame Rate (IFR) achievable with 4 parallel BFs. The IFR depends on the number of lines per frame, on the number of acquired points per line, and on the maximum analyzed depth. In this case we assumed 8 cm od depth (which is quite restrictive because during the receive time corresponding to 8 cm, i.e. about 100 μs, the processing is performed at the lower rate, F_S).

5.5. Tests and Results

In this section results obtained by Multi-line Parallel Beamformer implemented on ULA-OP 256 are presented. Two different strategies to obtain high-frame rate B-mode images are used. The first one uses plane wave to excite a large region of interest to collect and process the echoes backscattered form this large region. The second one, called Plane-Wave Compound imaging, sums coherently the points of several high frame rate plane wave images to achieve a single B-mode image with improved resolution and contrast, but lower frame rate [87].

5.5.1. Plane Wave Imaging

The echoes collected from a large region excited by a Plane Wave are used for simultaneously beamforming multiple lines of the B-mode image. The ULA-OP 256 system was connected to the 192-element probe LA533 (Esaote S.p.A, Florence, Italy). ULA-OP was programmed to transmit a plane wave burst (3-cycle at 8MHz) by using a 96-element aperture. The central 96-element aperture of the LA533 probe was selected for receiving. The MLBF was set to beamform frames of N = 96 lines. Since each FE of the system processes 32 lines, in this experiment 3 FEs were exploited in the RX processing. The number of analyzed depths was set to Np=2048, corresponding to about 2 cm of investigated depth. The working frequencies were F_S=78.125MHz and F_M=234.375MHz.

The investigation was performed by imaging the valve located in the femoral vein of a volunteer.

The valve keeps blood flowing toward the heart against the force of gravity and prevents the blood reflux. Only one of the 4 available BFs was here activated.

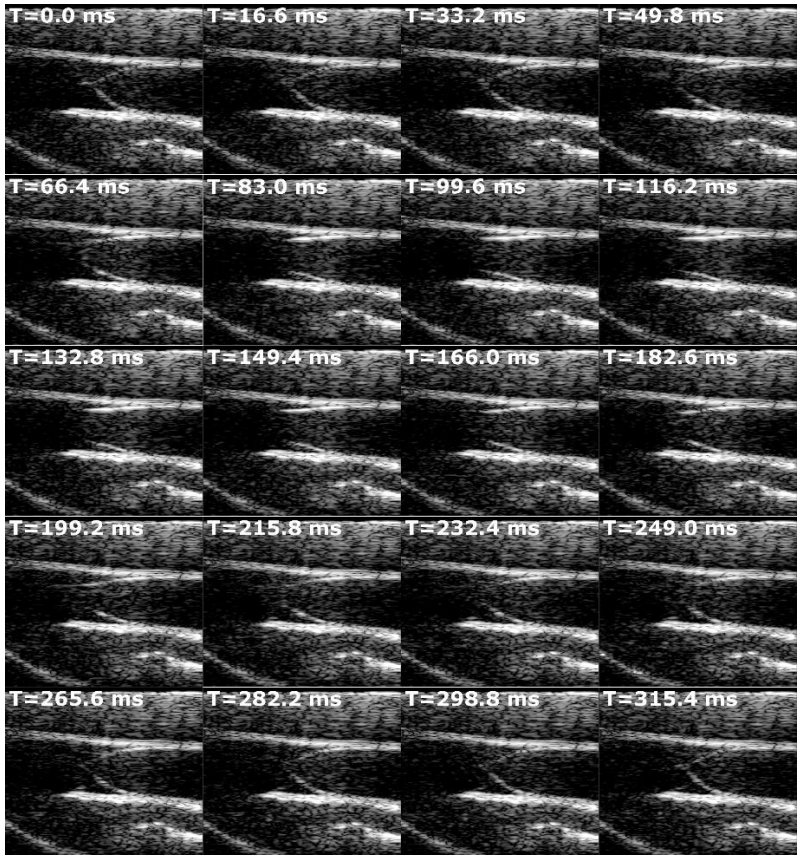

Fig. 85: The sequence of B-mode images show the details of the quick movement of a valve located in the femoral vein of a volunteer during its aperture-closure cycle. The original image sequence, obtained in real time at IFR =600Hz, is here decimated by factor 10. Each image is tagged with the corresponding time.

With *Np*=2048, *N*=96, F_S=78.125MHz and F_M =234.375MHz the BF could produce an IFR_m of more than 1000 Hz. However, we limited the output to T_{pri}= 1.66 ms, that corresponds to IFR_m= 600Hz, which was suitable for this application.

In Fig. 85, a selection of 20 screenshots, taken 1 frame out of 10 from the B-Mode movie, is reported. The details of the dynamics of the aperture and closure of the valve are clearly detected.

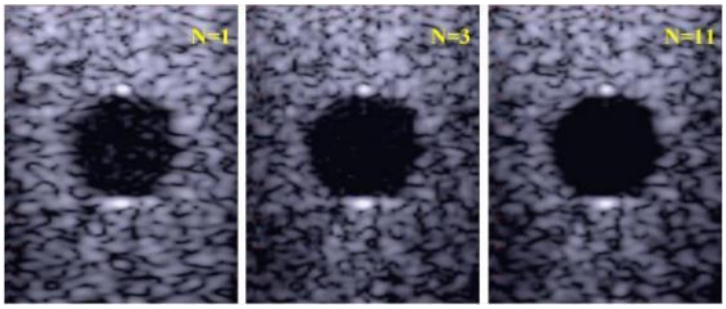

Fig. 86: Screenshots of the images reconstructed in real-time by the ULAOP 256 scanner, by compounding Ni=1, 3, 11 frames. The frame rate was 3000, 1000 and 270 Hz, respectively.

5.5.2. Plane-Wave Compound Imaging

The Plane-Wave Compound Imaging consists of coherent summation of several successive plane waves received from different angles. The plane waves are successively transmitted at different angles, and the received signals are summed coherently to improve resolution and contrast of the B-mode images obtained by plane-wave imaging. The ULA-OP 256 system was configured to transmit plane waves, at 3000 Hz PRF, by 64 active elements and to beamform a full image for each PRI. Thanks to the parallel beamforming, the system was able to generate fully reconstructed uncompounded images in real-time, at a frame rate equal to the PRF. To verify the correct execution of the real-time beamformer, B-Mode images (64 lines by 2048 depths) of a standard tissue mimicking phantom (Gammex 404GS, by Gammex, Middleton, WI) were reconstructed both without compounding (*Ni*=1) and by compounding 3 and 11 images (*Ni*=3, 11) with steering angles within ±7.5°. The resulting images (Fig. 86) where off-line analyzed to evaluate the Contrast Ratio (CR). As expected, CR actually increased with the number of compounded images and was estimated equal to 19.6dB, 23.1dB, and 29.5dB respectively.

5.6. Conclusion

In this chapter, we presented a Multi-Line Parallel beamforming architecture capable of improving the IFR of B-mode investigations in real-time. The proposed architecture was implemented and tested in FPGAs of the research echograph ULAOP-256. Running at F_M=234.375 MHz. It enabled real-time plane wave imaging with high frame rates, e.g. up to 3 kHz without compounding and 270 Hz when 11 frames were compounded.

The proposed Multi-Line Parallel Beamfromer was demonstrated capable of producing image sequences of good quality at IFR= 600Hz by plane wave imaging and Plane Wave compounding images at IFR =270Hz, suitable to detect quick movements of human tissues. The described parallel beamformer architecture is currently being used to test novel real-time multi-line transmit (MLT) methods for fast cardiac imaging [96], for real-time multi-line vector Doppler applications [97] and for fast ColorFlow Mapping applications [98].

5.7. Contributions on High Frame Rate Medical Imaging.

The presented work about High Frame Rate Medical Imaging has contributed to the follows scientific papers:

1. Boni, E., Bassi, L., Dallai, A., Guidi, F., **Meacci, V.**, Ramalli, A., Ricci, S., Tortoli, P.: ULA-OP 256: A 256-Channel Open Scanner for Development and Real-Time Implementation of New Ultrasound Methods. IEEE Transactions Ultrasonics and Ferroelectric, and Frequency Control. 63, 1488–1495 (2016).

2. Boni, E., Bassi, L., Dallai, A., Giannini, G., Guidi, F., **Meacci, V.**, Matera, R., Ramalli, A., Ricci, S., Scaringella, M., Viti, J., Tortoli, P.: ULA-OP 256: A portable high-performance research scanner. 2015 IEEE International Ultrasonics Symposium (IUS) Proceedings, pp. 1245-1248 (2015).

3. Boni, E., Bassi, L., Dallai, A., Giannini, G., Guidi, F., **Meacci, V.**, Ramalli, A., Ricci, S., Tortoli, P.: Open Platforms for the Advancement of Ultrasound Research. 2016 Applications in Electronics Pervading Industry, Environment and Society. pp. 59–64. Springer International Publishing (2016).

4. **Meacci, V.**, Bassi, L., Ricci, S., Boni, E., Tortoli, P.: Compact hardware for real-time multi-line beamforming. 2014 IEEE International Ultrasonics Symposium (IUS) Proceedings, pp. 1245-1248 (2014).

5. **Meacci, V.**, Bassi, L., Ricci, S., Boni, E., Tortoli, P.: High-Performance FPGA Architecture for Multi-line Beamforming in Ultrasound Applications. 2016 Euromicro Conference on Digital System Design (DSD). pp. 584–590 (2016).

6. Boni, E., Bassi, L., Dallai, A., **Meacci, V.**, Ramalli, A., Scaringella, M., Guidi, F., Ricci, S., Tortoli, P.: A real-time beamformer for high frame rate ultrasound imaging. 2016 IEEE International Ultrasonic Symposium (IUS) Proceedings, pp. 1–4 (2016).

7. Ramalli, A., Dallai, A., Boni, E., Bassi, L., **Meacci, V.**, Giovannetti, M., Tong, L., D'hooge, J., Tortoli, P.: Multi transmit beams for fast cardiac imaging towards clinical routine. 2016 IEEE International Ultrasonic Symposium (IUS) Proceedings, pp. 1–4 (2016).

8. Ricci, S., Bassi, L., **Meacci, V.**, Ramalli, A., Boni, E., Tortoli, P.: Multiline Measurements of Blood Velocity Vectors in Real-Time. 2016 IEEE International Ultrasonic Symposium (IUS) Proceedings, pp. 1–4 (2016).

The first one is the journal paper where the architecture of the ultrasound system ULA-OP 256 is explained in details in all its parts and some interesting applications are presented.
The second and third are conference proceedings where the evolution of the ULA-OP 256, the methods implemented on the system and results are presented and discussed.

The fourth , fifth and sixth are conference proceedings that report the evolution of the Multi-Line Parallel Beamformer. At the beginning the implementation on the previous version of the ultrasound scanner called ULA-OP, to demonstrate the potentiality of the method, then the evolution over the years until to reach the current version. Results are presented and discussed in each proceeding.

The fifth paper was presented at an international conference.

The seventh and eight are conference proceedings where two novel medical investigation methods implemented on ULA-OP 256 are described and results are discussed. The first one regards the transmission of multi focalized beams to beamform more lines for each Pulse Repetition Interval for increasing the Image Frame Rate. The second one concerns a method to represent the blood flow in the vessel by using vectors with different colors, useful to understand the extremely complexity of the blood flow inside the vessels and reveal diseases.
All contributions are reported in section 1.2.

Chapter 6. Conclusion

This chapter summarizes the contribution of the thesis and discusses possible directions for future research.

6.1. Summary of Contributions

This PhD project introduces innovative ultrasound systems and investigation techniques for ultrasound imaging in medical and industrial fields.

Two pulse wave ultrasound systems designed for industrial applications were developed:

The first one evaluates the concrete strength during the hydration process. It embeds all the electronics needed to acquire, save and move data to a host. Experiments were presented that showed the good accuracy of the measurements performed during all of the phases of the concrete hardening process. The capacity of the system to autonomously run by batteries for days and the simple setup make this an ideal instrument for on-site application. Some prototypes of the system were produced and are currently being tested in real on-field applications.

The second one is a crucial component of an integrated digital in-line fluids characterization system for industrial and research applications. The electronics includes on-board powerful programmable devices to process in real-time the velocity profile of fluids flowing in pipes. The possibility to acquire data at 100 MHz guarantees a very high spatial resolution, while the low noise approach allows the system to work also in attenuating fluids. The system has been successfully tested in a wide range of industrial applications, e.g. oil, petroleum, food, minerals, chocolate, explosive emulsions, pharmaceutical industry.

Concerning biomedical applications, a novel beamforming architecture, called Multi-Line Parallel beamforming, has been presented. It was implemented in the FPGAs of the research scanner ULA-OP256. The Multi-Line Parallel Beamformer exploits a combination of parallel and serial technique able to produce High Frame rate and compounded B-Mode images in real-time, suitable to detect quick movements of human tissues. The proposed beamformer is currently being used to test novel investigation methods as real-time multi-line transmit (MLT), real-time multi-line vector Doppler applications and for fast ColorFlow Mapping applications.

6.2. Direction of Future Works

The Future works consist of:

- Designing of low power version of the system to assess the concrete strength. It will include a Wi-Fi connection and will feature a web interfaced. The main application will be evaluating concrete strength on field for months, running by batteries.
- New features for the system used to characterize opaque fluids will be added in a next version of the firmware. The goal is to control separately the two channels managed by the electronics. This allows the system to transmit and acquire two signals with different frequency and amplitude.
- A wide range of works are in progress On ULA-OP 256:
  Implementation of new investigation methods as Multi Line Transmit and receive, Multi Line Vector Doppler, Color Flow etc. are under test.
  Soon C-MUT probes will be tested to investigate their properties and capabilities.
  Adding a Ping-Pong buffer that consists in splitting the dual port memory used for storing the acquired data in two blocks. The first one will be used for storing the acquired data in current PRI and the other for processing the data acquired during the previous PRI. In this way, the system acquires and beamforms the data at same time and the down time between acquisitions decreases.

Bibliography

[1] T. Szabo, *Diagnostic Ultrasound Imaging: Inside Out*, 2nd Edition. Elsevier.
[2] B. D. Steinberg, "Digital beamforming in ultrasound," *IEEE Trans. Ultrason. Ferroelectr. Freq. Control*, vol. 39, no. 6, pp. 716–721, Nov. 1992.
[3] Z. Li, *Advanced concrete technology*. Hoboken, N.J: Wiley, 2011.
[4] T. C. Powers and T. L. Brownyard, *Studies of the physical properties of hardened portland cement paste:* Chicago, 1948.
[5] S. P. Jiang, J. C. Mutin, and A. Nonat, "Studies on mechanism and physico-chemical parameters at the origin of the cement setting. I. The fundamental processes involved during the cement setting," *Cem. Concr. Res.*, vol. 25, no. 4, pp. 779–789, 1995.
[6] D. Lootens and D. P. Bentz, "On the relation of setting and early-age strength development to porosity and hydration in cement-based materials," *Cem. Concr. Compos.*, vol. 68, pp. 9–14, Apr. 2016.
[7] D. P. Bentz, "Cement hydration: Building bridges and dams at the microstructure level," *Mater. Struct. Constr.*, vol. 40, no. 4, pp. 397–404, 2007.
[8] D. P. Bentz, T. Barrett, I. De la Varga, and W. J. Weiss, "Relating compressive strength to heat release in mortars," *Adv. Civ. Eng. Mater.*, vol. 1, no. 1, pp. 1–14, 2012.
[9] D. P. Bentz, "Influence of water-to-cement ratio on hydration kinetics: Simple models based on spatial considerations," *Cem. Concr. Res.*, vol. 36, no. 2, pp. 238–244, 2006.
[10] D. P. Bentz, M. A. Peltz, and J. Winpigler, "Early-age properties of cement-based materials. II: Influence of water-to-cement ratio," *J. Mater. Civ. Eng.*, vol. 21, no. 9, pp. 512–517, 2009.
[11] T. Powers, "Absorption of Water by Portland Cement Paste during the Hardening Process," *Ind. Eng. Chem.*, vol. 27, no. 7, pp. 790–794, Jul. 1935.
[12] B. Lindlar and M. Jahn, "Method Statement Strength Measurement of Shotcrete," Tüffenwies 16, CH-8048 Zürich, Switzerland, 03-Oct-2010.
[13] Snehal P.Abhyankar and Shekhar D. Bhole, "Electrical Properties And Compressive Strength of Concrete With SCMs and COIRS," *Int. J. Adv. Technol. Civ. Eng.*, vol. 1, 2012.
[14] A. Boumiz, C. Vernet, and F. C. Tenoudji, "Mechanical properties of cement pastes and mortars at early ages," *Adv. Cem. Based Mater.*, vol. 3, no. 3, pp. 94–106, Apr. 1996.
[15] T. Voigt, Y. Akkaya, and S. P. Shah, "Determination of early age mortar and concrete strength by ultrasonic wave reflections," *J. Mater. Civ. Eng.*, vol. 15, no. 3, pp. 247–254, 2003.

[16] T. Voigt, Z. Sun, and S. P. Shah, "Comparison of ultrasonic wave reflection method and maturity method in evaluating early-age compressive strength of mortar," *Cem. Concr. Compos.*, vol. 28, no. 4, pp. 307–316, 2006.

[17] K. V. Subramaniam, J. Lee, and B. J. Christensen, "Monitoring the setting behavior of cementitious materials using one-sided ultrasonic measurements," *Cem. Concr. Res.*, vol. 35, no. 5, pp. 850–857, 2005.

[18] N. Robeyst, C. U. Grosse, and N. D. Belie, "Relating ultrasonic measurements on fresh concrete with mineral additions to the microstructure development simulated by Cemhyd3D," *Cem. Concr. Compos.*, vol. 33, no. 6, pp. 680–693, 2011.

[19] S. Popovics and J. S. Popovics, "Ultrasonic Testing to Determine Water-Cement Ratio for Freshly Mixed Concrete," *Cem. Concr. Aggreg.*, vol. 20, no. 2, pp. 262–268, 1998.

[20] C. M. Sayers and A. Dahlin, "Propagation of ultrasound through hydrating cement pastes at early times," *Adv. Cem. Based Mater.*, vol. 1, no. 1, pp. 12–21, Oct. 1993.

[21] T. Gudra and B. Stawiski, "Non-destructive strength characterization of concrete using surface waves," *Ndt E Int.*, vol. 33, no. 1, pp. 1–6, 2000.

[22] Y. Akkaya, T. Voigt, K. V. Subramaniam, and S. P. Shah, "Nondestructive measurement of concrete strength gain by an ultrasonic wave reflection method," *Mater. Struct.*, vol. 36, no. 8, pp. 507–514.

[23] M. I. Valič, "Hydration of cementitious materials by pulse echo USWR: method, apparatus and application examples," *Cem. Concr. Res.*, vol. 30, no. 10, pp. 1633–1640, 2000.

[24] L. Oblak, B. Lindlar, and D. Lootens, "Continuous Monitoring of Strength Evolution of Shotcrete," presented at the Spritzbeton Tagung-2012, Alpbach, Austria, 2012.

[25] B. Graybeal, "Compression Response of a Rapid-Strengthening Ultra-High Performance Concrete Formulation," *Report No. FHWA-HRT-06-103, Federal Highway Administration, Washington, DC*, Sep-2012.

[26] D. Lootens, P. Jousset, L. Martinie, N. Roussel, and R. J. Flatt, "Yield stress during setting of cement pastes from penetration tests," *Cem. Concr. Res.*, vol. 39, no. 5, pp. 401–408, 2009.

[27] R. D'Angelo, T. J. Plona, L. M. Schwartz, and P. Coveney, "Ultrasonic measurements on hydrating cement slurries," *Adv. Cem. Based Mater.*, vol. 2, no. 1, pp. 8–14, Jan. 1995.

[28] D. Lootens, J. L. Rios, R. Flatt, and N. Blank, "Device and Method for Determining the Dynamic Elastic Modulus of a Material," US20090205427 A1, 20-Aug-2009.

[29] "EN 55011:2009-11 Industrial, scientific and medical equipment - Radio-frequency disturbance characteristics - Limits and methods of measurement." 2013.

[30] F. Nilenius, F. Larsson, K. Lundgren, and K. Runesson, "Computational homogenization of diffusion in three-phase mesoscale concrete," *Comput. Mech.*, vol. 54, no. 2, pp. 461–472, Mar. 2014.

[31] T. Fan, "Concrete microstructure homogenization technique with application to model concrete serviceability," 2012.

[32] J. M. Dealy and K. F. Wissbrun, *Melt Rheology and Its Role in Plastics Processing*. Dordrecht: Springer Netherlands, 1990.

[33] Christopher W. Macosko, *Rheology: Principles, Measurements, and Applications*. 1994.

[34] R.P. Chhabra and J.F. Richardson, *Non-newtonian flow in the process industries: Fundamentals and engineering applications*, 1st Edition., vol. 79. Butterworth-Heinemann, Oxford, UK, 1999.

[35] S. Ricci, E. Boni, F. Guidi, T. Morganti, and P. Tortoli, "A programmable real-time system for development and test of new ultrasound investigation methods," *IEEE Trans. Ultrason. Ferroelectr. Freq. Control*, vol. 53, no. 10, pp. 1813–1819, Oct. 2006.

[36] "Measurement, Instrumentation, and Sensors Handbook, Second Edition: Spatial, Mechanical, Thermal, and Radiation Measurement," *CRC Press*, 29-Jan-2014. [Online]. Available: https://www.crcpress.com/Measurement-Instrumentation-and-Sensors-Handbook-Second-Edition-Spatial/Webster-Eren/p/book/9781439848883. [Accessed: 05-Nov-2016].

[37] I. Roberts, "In-line and online rheology measurement," Kress-Rogers & Brimelow (eds), Instrumentation and sensors for the food industry. 2° ed. Woodhead Publishing Limited, Abington Hall, Cambridge, 2001, pp. 403–419.

[38] J. Wiklund, I. Shahram, and M. Stading, "Methodology for in-line rheology by ultrasound Doppler velocity profiling and pressure difference techniques," *Chem. Eng. Sci.*, vol. 62, no. 16, pp. 4277–4293, Aug. 2007.

[39] M. Mueller, P. O. Brunn, and T. Wunderlich, "New rheometric technique: the gradient-ultrasound pulse Doppler method," *Appl. Rheol.*, vol. 7, no. 5, pp. 204–210, 1997.

[40] N. Dogan, M. J. McCarthy, and R. L. Powell, "In-line measurement of rheological parameters and modeling of apparent wall slip in diced tomato suspensions using ultrasonics," *J. Food Sci.*, vol. 67, no. 6, pp. 2235–2240, 2002.

[41] J. Wiklund, R. Kotzé, R. Haldenwang, and M. Stading, "Development of an industrial UVP+PD based rheometer - optimisation of UVP system and transducer technology," presented at the 8th International Symposium on Ultrasonic Doppler Methods for Fluid Mechanics and Fluid Engineering, 2012, pp. 49–52.

[42] J. Wiklund *et al.*, "In-Line Ultrasound based Rheometry of industrial and model suspensions flowing through pipes," in *ResearchGate*, 2002.

[43] Y. Takeda, "Development of an ultrasound velocity profile monitor," *Nucl. Eng. Des.*, vol. 126, no. 2, pp. 277–284, Apr. 1991.

[44] B. Ouriev and E. J. Windhab, "Rheological study of concentrated suspensions in pressure-driven shear flow using a novel in-line ultrasound Doppler method," *Exp. Fluids*, vol. 32, no. 2, pp. 204–211.

[45] T. Wunderlich and P. O. Brunn, "Ultrasound pulse Doppler method as a viscometer for process monitoring," *Flow Meas. Instrum.*, vol. 10, no. 4, pp. 201–205, Dec. 1999.

[46] R. Kotzé, R. Haldenwang, and P. Slatter, "Rheological characterization of highly concentrated mineral suspensions using ultrasound velocity profiling with combined pressure difference method," vol. 18, no. 6, pp. 62114-1-62114–10, Jan. 2008.

[47] Kowalewski TA, "Velocity profiles of suspension flowing through a tube," pp. 857–865, 1980.

[48] S. Ricci, M. Liard, B. Birkhofer, D. Lootens, A. Bruhwiler, and P. Tortoli, "Embedded Doppler system for industrial in-line rheometry," *IEEE Trans. Ultrason. Ferroelectr. Freq. Control*, vol. 59, no. 7, pp. 1395–1401, Jul. 2012.

[49] S. Ricci, B. Birkhofer, D. Lootens, and P. Tortoli, "In-line rheometry for highly filled suspensions through Doppler ultrasound," presented at the Proceedings - IEEE Ultrasonics Symposium, 2010, pp. 2044–2047.

[50] M. Vogt, "Direct sampling and baseband conversion in doppler systems for high-frequency ultrasound blood flow measurements," *Electron. Lett.*, vol. 41, no. 14, pp. 789–790, 2005.

[51] J. Wiklund *et al.*, "Flow-VizTM–A fully integrated and commercial in-line fluid characterization system for industrial applications," in *Proceedings of the 9th International Symposium on Ultrasonic Doppler Methods for Fluid Mechanics and Fluid Engineering*, 2014, p. 105.

[52] J. Wiklund and M. Stading, "Application of in-line ultrasound Doppler-based UVP-PD rheometry method to concentrated model and industrial suspensions," *Flow Meas. Instrum.*, vol. 19, no. 3–4, pp. 171–179, 2008.

[53] R. Kotzé, J. Wiklund, and R. Haldenwang, "Optimisation of Pulsed Ultrasonic Velocimetry system and transducer technology for industrial applications," *Ultrasonics*, vol. 53, no. 2, pp. 459–469, Feb. 2013.

[54] R. Kotzé, S. Ricci, B. Birkhofer, and J. Wiklund, "Performance tests of a new non-invasive sensor unit and ultrasound electronics," *Flow Meas. Instrum.*, vol. 48, pp. 104–111, Apr. 2016.

[55] S. Ricci, M. Cinthio, T. R. Ahlgren, and P. Tortoli, "Accuracy and Reproducibility of a Novel Dynamic Volume Flow Measurement Method," *Ultrasound Med. Biol.*, vol. 39, no. 10, pp. 1903–1914, 2013.

[56] S. Ricci, V. Meacci, B. Birkhofer, and J. Wiklund, "Embedded system for in-line ultrasound velocity profile detection," in *Ultrasonics Symposium (IUS), 2015 IEEE International*, 2015, pp. 1–4.

[57] B. Birkhofer, A. Debacker, S. Russo, S. Ricci, and D. Lootens, "In-line rheometry based on ultrasonic velocity profiles: comparison of data processing methods," vol. 22, no. 4, 2012.

[58] M. Pollakowski and H. Ermert, "Chirp Signal Matching and Signal Power Optimization in Pulse-Echo Mode Ultrasonic Nondestructive Testing," *IEEE Trans. Ultrason. Ferroelectr. Freq. Control*, vol. 41, no. 5, pp. 655–659, 1994.

[59] P. Tortoli and J. A. Jensen, "Introduction to the Special Issue on Novel Equipment for Ultrasound Research," *IEEE Trans. Ultrason. Ferroelectr. Freq. Control*, vol. 53, no. 10, pp. 1705–1706, Oct. 2006.

[60] J. A. Jensen *et al.*, "SARUS: A synthetic aperture real-time ultrasound system," *IEEE Trans. Ultrason. Ferroelectr. Freq. Control*, vol. 60, no. 9, pp. 1838–1852, 2013.

[61] C. C. P. Cheung *et al.*, "Multi-channel pre-beamformed data acquisition system for research on advanced ultrasound imaging methods," *IEEE Trans. Ultrason. Ferroelectr. Freq. Control*, vol. 59, no. 2, pp. 243–253, 2012.

[62] "Supersonic Imagine. (2013). Aixplorer." [Online]. Available: http://ww.w.supersonicimagine.com/Aixplorer-R/ Technology. [Accessed: 23-Jan-2013].

[63] "Verasonics Inc. (2012). Technology Overview." [Online]. Available: http://verasonics.com/the-vantage-advantage/. [Accessed: 02-Feb-2016].

[64] M. Lewandowski, M. Walczak, B. Witek, P. Kulesza, and K. Sielewicz, "Modular & scalable ultrasound platform with GPU processing," presented at the IEEE International Ultrasonics Symposium, IUS, 2012.

[65] E. Boni *et al.*, "A reconfigurable and programmable FPGA-based system for nonstandard ultrasound methods," *IEEE Trans. Ultrason. Ferroelectr. Freq. Control*, vol. 59, no. 7, pp. 1378–1385, 2012.

[66] P. Tortoli, A. Dallai, E. Boni, L. Francalanci, and S. Ricci, "An Automatic Angle Tracking Procedure for Feasible Vector Doppler Blood Velocity Measurements," *Ultrasound Med. Biol.*, vol. 36, no. 3, pp. 488–496, 2010.

[67] S. Ricci, L. Bassi, and P. Tortoli, "Real-time vector velocity assessment through multigate doppler and plane waves," *IEEE Trans. Ultrason. Ferroelectr. Freq. Control*, vol. 61, no. 2, pp. 314–324, 2014.

[68] M. Lenge, A. Ramalli, E. Boni, H. Liebgott, C. Cachard, and P. Tortoli, "High-frame-rate 2-D vector blood flow imaging in the frequency domain," *IEEE Trans. Ultrason. Ferroelectr. Freq. Control*, vol. 61, no. 9, pp. 1504–1514, 2014.

[69] P. Tortoli, M. Lenge, D. Righi, G. Ciuti, H. Liebgott, and S. Ricci, "Comparison of carotid artery blood velocity measurements by vector and standard doppler approaches," *Ultrasound Med. Biol.*, vol. 41, no. 5, p. 1354–1362, 2015.

[70] O. Lorintiu, H. Liebgott, and D. Friboulet, "Compressed Sensing Doppler Ultrasound Reconstruction Using Block Sparse Bayesian Learning," *IEEE Trans. Med. Imaging*, vol. 35, no. 4, pp. 978–987, 2016.

[71] M. Alessandrini *et al.*, "A new technique for the estimation of cardiac motion in echocardiography based on transverse oscillations: A preliminary evaluation in silico and a feasibility demonstration in vivo," *IEEE Trans. Med. Imaging*, vol. 33, no. 5, pp. 1148–1162, 2014.

[72] L. Tong *et al.*, "Wide-angle tissue doppler imaging at high frame rate using multi-line transmit beamforming: An experimental validation In Vivo," *IEEE Trans. Med. Imaging*, vol. 35, no. 2, pp. 521–528, 2016.

[73] A. R. Ahlgren *et al.*, "Profound increase in longitudinal displacements of the porcine carotid artery wall can take place independently of wall shear stress: A continuation report," *Ultrasound Med. Biol.*, vol. 41, no. 5, pp. 1342–1353, 2015.

[74] S. Salles *et al.*, "Plane wave transverse oscillation (PWTO): An ultra-fast transverse oscillation imaging mode performed in the Fourier domain for 2D motion estimation of the carotid artery," presented at the 2014 IEEE 11th International Symposium on Biomedical Imaging, ISBI 2014, 2014, pp. 1409–1412.

[75] F. Varray, A. Ramalli, C. Cachard, P. Tortoli, and O. Basset, "Fundamental and second-harmonic ultrasound field computation of inhomogeneous nonlinear medium with a generalized angular spectrum method," *IEEE Trans. Ultrason. Ferroelectr. Freq. Control*, vol. 58, no. 7, pp. 1366–1376, 2011.

[76] L. Demi, S. Van, H. Wijkstra, and M. Mischi, "Cumulative phase delay imaging for contrast-enhanced ultrasound tomography," *Phys. Med. Biol.*, vol. 60, no. 21, pp. L26–L33, 2015.

[77] F. Lin, C. Cachard, R. Mori, F. Varray, F. Guidi, and O. Basset, "Ultrasound contrast imaging: Influence of scatterer motion in multi-pulse techniques," *IEEE Trans. Ultrason. Ferroelectr. Freq. Control*, vol. 60, no. 10, pp. 2065–2078, 2013.

[78] S. Salles, H. Liebgott, O. Basset, C. Cachard, D. Vray, and R. Lavarello, "Experimental evaluation of spectral-based quantitative ultrasound imaging using plane wave compounding," *IEEE Trans. Ultrason. Ferroelectr. Freq. Control*, vol. 61, no. 11, pp. 1824–1834, 2014.

[79] A. Ramalli, O. Basset, C. Cachard, E. Boni, and P. Tortoli, "Frequency-domain-based strain estimation and high-frame-rate imaging for quasi-static elastography," *IEEE Trans. Ultrason. Ferroelectr. Freq. Control*, vol. 59, no. 4, pp. 817–824, 2012.

[80] M. Toulemonde, O. Basset, P. Tortoli, and C. Cachard, "Thomson's multitaper approach combined with coherent plane-wave compounding to reduce speckle in ultrasound imaging," *Ultrasonics*, vol. 56, pp. 390–398, 2015.

[81] G. Matrone, A. S. Savoia, G. Caliano, and G. Magenes, "The delay multiply and sum beamforming algorithm in ultrasound B-mode medical imaging," *IEEE Trans. Med. Imaging*, vol. 34, no. 4, pp. 940–949, 2015.

[82] K. Shapoori, J. Sadler, A. Wydra, E. V. Malyarenko, A. N. Sinclair, and R. G. Maev, "An ultrasonic-adaptive beamforming method and its application for trans-skull imaging of certain types of head injuries; Part I: Transmission mode," *IEEE Trans. Biomed. Eng.*, vol. 62, no. 5, pp. 1253–1264, 2015.

[83] A. Wydra, E. Malyarenko, K. Shapoori, and R. G. Maev, "Development of a practical ultrasonic approach for simultaneous measurement of the thickness and the sound speed in human skull bones: A laboratory phantom study," *Phys. Med. Biol.*, vol. 58, no. 4, pp. 1083–1102, 2013.

[84] K. Shapoori *et al.*, "Ultrasonic imaging of foreign inclusions and blood vessels through thick skull bones," *Mil. Med.*, vol. 180, no. 3, pp. 104–108, 2015.

[85] M. Gyöngy and Á. Makra, "Experimental validation of a convolution-based ultrasound image formation model using a planar arrangement of micrometer-scale scatterers," *IEEE Trans. Ultrason. Ferroelectr. Freq. Control*, vol. 62, no. 6, pp. 1211–1219, 2015.

[86] J.-Y. Lu, "2D and 3D High Frame Rate Imaging with Limited Diffraction Beams," *IEEE Trans. Ultrason. Ferroelectr. Freq. Control*, vol. 44, no. 4, pp. 839–856, 1997.

[87] G. Montaldo, M. Tanter, J. Bercoff, N. Benech, and M. Fink, "Coherent plane-wave compounding for very high frame rate ultrasonography and transient elastography," *IEEE Trans. Ultrason. Ferroelectr. Freq. Control*, vol. 56, no. 3, pp. 489–506, 2009.

[88] I. Trots, A. Nowicki, M. Lewandowski, and Y. Tasinkevych, *Synthetic aperture method in ultrasound imaging*. INTECH Open Access Publisher, 2011.

[89] D. H. Evans and W. N. McDicken, *Doppler Ultrasound: Physics, Instrumentation and Signal Processing*, 2nd Edition. Wiley, 1999.

[90] H. Hasegawa and H. Kanai, "High-frame-rate echocardiography using diverging transmit beams and parallel receive beamforming," *J. Med. Ultrason.*, vol. 38, no. 3, pp. 129–140, May 2011.

[91] R. Shekhar, V. Zagrodsky, M. J. Garcia, and J. D. Thomas, "Registration of real-time 3-D ultrasound images of the heart for novel 3-D stress echocardiography," *IEEE Trans. Med. Imaging*, vol. 23, no. 9, pp. 1141–1149, Sep. 2004.

[92] O. T. von Ramm, S. W. Smith, and H. G. Pavy, "High-speed ultrasound volumetric imaging system. II. Parallel processing and image display," *IEEE Trans. Ultrason. Ferroelectr. Freq. Control*, vol. 38, no. 2, pp. 109–115, Mar. 1991.

[93] J. Bercoff *et al.*, "Ultrafast compound doppler imaging: providing full blood flow characterization," *IEEE Trans. Ultrason. Ferroelectr. Freq. Control*, vol. 58, no. 1, pp. 134–147, Jan. 2011.

[94] E. Boni, A. Cellai, A. Ramalli, M. Lenge, and S. Ricci, "Multi-channel Raw-Data Acquisition for Ultrasound Research," in *2014 17th Euromicro Conference on Digital System Design (DSD)*, 2014, pp. 647–650.

[95] B. Y. S. Yiu, I. K. H. Tsang, and A. C. H. Yu, "GPU-based beamformer: Fast realization of plane wave compounding and synthetic aperture imaging," *IEEE Trans. Ultrason. Ferroelectr. Freq. Control*, vol. 58, no. 8, pp. 1698–1705, Aug. 2011.

[96] A. Ramalli *et al.*, "Multi transmit beams for fast cardiac imaging towards clinical routine," presented at the 2016 IEEE Ultrasonics Symposium., 2016.

[97] S. Ricci, L. Bassi, V. Meacci, A. Ramalli, E. Boni, and P. Tortoli, "Multiline Measurements of Blood Velocity Vectors in Real-Time," presented at the 2016 IEEE Ultrasonics Symposium., 2016.

[98] F. Guidi, A. Dallai, E. Boni, A. Ramalli, and P. Tortoli, "Implementation of color-flow plane-wave imaging in real-time," presented at the 2016 IEEE Ultrasonics Symposium., 2016.